ARTICLE OPEN

Check for updates

Oxidative dissolution of $(U,Ce)O_2$ materials in aqueous solutions containing H_2O_2

Théo Montaigne[1], Stéphanie Szenknect[1]✉, Véronique Broudic[2], Paul-Henri Imbert[1], Florent Tocino[3], Christelle Martin[4], Frédéric Miserque[5], Christophe Jégou[2]✉ and Nicolas Dacheux[1]

Homogeneous and heterogeneous $U_{1-x}Ce_xO_2$ (with $0 \leq x \leq 0.25$) materials were prepared via wet and dry chemistry routes, respectively before being submitted to dynamic leaching experiments. The feeding solution containing 0.20 mmol.L^{-1} H_2O_2 was kept under air and renewed to guarantee the stability of H_2O_2 during the experiment. Normalized alteration rates were determined from U concentration in the leachates. For homogeneous $(U,Ce)O_2$ materials, the dissolution rate was divided by a factor of 3 when increasing the Ce content from 0.08 to 0.25. Surface characterizations revealed that studtite precipitated all over UO_2 pellet surface and only on the UO_2 grains of heterogeneous $U_{0.92}Ce_{0.08}O_2$ samples. The behaviour of this heterogeneous material was similar to that observed for $(U,Pu)O_2$ in the same conditions, which revealed the reliability of cerium as a plutonium analogue.

npj Materials Degradation (2023)7:34; https://doi.org/10.1038/s41529-023-00348-3

INTRODUCTION

Direct disposal of UO_2 and Mixed OXide (MOX) spent fuel in a deep geological repository is being studied in many countries as a possible way to manage high-level radioactive waste[1–5]. Although the reprocessing of spent fuel remains the reference option in France[6], the direct disposal is also studied as an option within the framework of the French national plan for the management of radioactive waste. This is especially the case for MOX spent fuel for which the option of multi-recycling in Pressurized Water Reactor (PWR) is under investigation, as is the possibility of direct disposal. This last option requires a detailed understanding of the interactions between spent fuel and water to establish very long-term evolution models and extrapolations.

For UO_2-based spent fuel, the key mechanism controlling the dissolution of uranium dioxide and the concomitant release of radionuclides from the ceramic is an oxidizing dissolution induced by the inherent radioactivity of the fuel and water radiolysis[7]. Even if the repository sites selected to date present a reducing environment (granitic bedrock for the KBS-3 Swedish design, Callovian-Oxfordian COx or Boom clays for France and Belgium…) ensuring low uranium solubility[1], the production of oxidizing radiolytic species can disturb the redox potential at the UO_2/water interface and lead to local oxidizing conditions[2]. Such oxidizing conditions can induce an increase of the uranium solubility by several orders of magnitude. The oxidative dissolution of UO_2 has been the subject of many studies both on radioactive and non-radioactive materials[8–10] and in more or less complex media (carbonated water, groundwater, with and without electroactive species like iron and hydrogen, etc.)[11–18]. It is now admitted[19] that hydrogen peroxide, produced by the radiolysis of water, is the main oxidizing species controlling the oxidation kinetics of UO_2. Moreover, the formation of uranium peroxide in the presence of hydrogen peroxide produced by the radiolysis of water or added in solution has been the subject of many observations both on UOX spent fuel[20–22] and on UO_2 model systems[10,23,24]. The crystallography of these peroxides (studtite, metastudtite) is well documented[25] and they can have different morphologies (needle-like crystals, nanoclusters…)[24,26] depending on the precipitation conditions. In addition, the presence of electroactive species such as iron and hydrogen produced by the anoxic corrosion of canisters can inhibit the oxidative dissolution of the fuel matrix and limit the mobility of redox-sensitive radionuclides[14].

Although UO_2 spent fuel alteration mechanisms have been described in the literature, it is not the case when considering $U_{1-x}Pu_xO_2$ fuels and especially, Mimas® MOX fuels. This kind of fuel, industrially produced after reprocessing of UO_2-based spent fuel, is characterized by a heterogeneous microstructure and variable plutonium contents[27,28]. The oxidative dissolution may be affected by microstructure and plutonium content. Indeed, plutonium is reported to stabilize the fluorite structure with respect to oxidation[29–31]. Moreover, plutonium exhibits different oxidation states likely to affect the processes of catalytic decomposition of hydrogen peroxide[32] and the nature of the secondary phases/altered layers at the interface. In this context, it is particularly important to assess the effect of hydrogen peroxide on the oxidative dissolution of MIMAS® MOX fuels. Furthermore, the use of a non-radioactive surrogate material with comparable properties to Pu reflects relevant practical advantages of being non-active; making handling far easier, i.e. without any troublesome issues and handling constraints accompanying a direct use of PuO_2. As such, the choice of suitable surrogate materials allowing multi-parametric studies without constraints of use is a major challenge for improving our knowledge of the alteration of MIMAS® MOX fuels. Potential candidates incorporate cerium, as a plutonium surrogate. Indeed, CeO_2 is extensively used as a surrogate for PuO_2 in MOX fuel development since the analogy between the (U-Pu-O) and (U-Ce-O) ternary phase diagrams has been established[33,34]. The similarities between the crystallographic (Supplementary Table 1) and the thermodynamic properties of the U-Ce-O and U-Pu-O systems makes their oxidation and phase behavior quite comparable[35]. However, if the analogy between the two systems has been validated for MOX fuel

[1]ICSM, Univ Montpellier, CNRS, CEA, ENSCM, Site de Marcoule, Bagnols/Cèze, France. [2]CEA, DES, ISEC, DE2D, Univ Montpellier, Marcoule, France. [3]EDF R & D, les Renardières, 77818 Moret-sur-Loing, France. [4]ANDRA, R & D Division, 1/7 rue Jean Monnet, 92298 Châtenay-Malabry, France. [5]Université Paris-Saclay, CEA, DES, SCCME, 91191 Gif-sur-Yvette, France. ✉email: stephanie.szenknect@cea.fr; christophe.jegou@cea.fr

Table 1. Powdered materials properties.

Raw powder	$UO_{2+\delta}$	$U_{0.92}Ce_{0.08}O_{2\pm\delta}$ heterogeneous	$U_{0.92}Ce_{0.08}O_{2\pm\delta}$	$U_{0.88}Ce_{0.12}O_{2\pm\delta}$	$U_{0.75}Ce_{0.25}O_{2\pm\delta}$
x_{Ce} theoretical	0	0.08	0.08	0.12	0.25
x_{Ce} measured	/	/	0.075 ± 0.006	0.111 ± 0.002	0.248 ± 0.008
Lattice parameter (Å)	5.465(1)	/	5.446(2)	5.455(1)	5.438(3)
Specific surface area ($m^2.g^{-1}$)	21 ± 1	16 ± 1	27 ± 1	9 ± 1	34 ± 1
Crystallite size (nm) XRD	20 ± 1	/	15 ± 1	36 ± 1	9 ± 1

Table 2. Sintered pellets properties after sintering at 1600 °C under Ar-H_2 4.5% for several hours.

Sintered pellets	$UO_{2+\delta}$	$U_{0.92}Ce_{0.08}O_{2\pm\delta}$ heterogeneous	$U_{0.92}Ce_{0.08}O_{2\pm\delta}$	$U_{0.88}Ce_{0.12}O_{2\pm\delta}$	$U_{0.75}Ce_{0.25}O_{2\pm\delta}$
Pellet mass (mg)	121.9 ± 0.1	86.2 ± 0.1	93.6 ± 0.1	51.0 ± 0.1	79.4 ± 0.1
Geometric surface area (10^{-5} m²)	2.9 ± 0.1	2.9 ± 0.1	2.6 ± 0.1	2.5 ± 0.1	2.7 ± 0.1
Lattice parameter (Å)	5.469(3)	/	5.465(2)	5.462(3)	5.456(1)
$\rho_{calculated}$ ($g.cm^{-3}$)	10.96 ± 0.02	/	10.69 ± 0.01	10.56 ± 0.02	10.05 ± 0.01
Geometric densification rate (%)	95 ± 2	88 ± 2	98 ± 2	96 ± 2	97 ± 2
Pycnometric densification rate (%)	97 ± 1	98 ± 1	98 ± 1	99 ± 1	97 ± 1
Opened porosity (%)	2 ± 1	9 ± 1	1 ± 1	1 ± 1	1 ± 1
Closed porosity (%)	3 ± 1	2 ± 1	2 ± 1	3 ± 1	3 ± 1
Grain average size (µm)	10 ± 6	≤1 (UO_2) 5–10 ((U, Ce)O_2)	5 ± 2	5 ± 2	6 ± 3

fabrication, thermal and sintering behavior[36–39], there is little evidence in the literature for similar alteration mechanism in aqueous solutions (at the noticeable exception of dissolution in concentrated nitric acid solutions[40–42]). It is noteworthy that the Ce(IV) and Pu(IV) standard hydrolysis constants are close and the solubility of the two MO_2 oxides very low (Supplementary Table 1). Nevertheless, one of the main discrepancy in the chemical properties of the two elements is the value of the standard redox potential of the M^{4+}/M^{3+} couple[43], which differs significantly and can affect the speciation of Ce and Pu in solution.

Therefore, this work aims at studying the oxidative dissolution of $U_{1-x}Ce_xO_2$ surrogate materials in the presence of hydrogen peroxide. These materials incorporate cerium at different concentrations and exhibit various microstructures. The goal of this study is to evaluate the influence of these parameters (cerium contents and microstructure) on the oxidative dissolution of MOX fuels but also to investigate the analogy with plutonium mixed oxides in these conditions.

RESULTS

Characterization of mixed oxides powders and sintered pellets

Physico-chemical properties of the raw powders were determined by elemental analyses, XRD and N_2 adsorption isotherms (Table 1). Measured Ce contents were found to be close to the theoretical values, if not exactly the same within the uncertainties for every homogeneous material. Specific surface areas were in the range of 9–35 m^2/g for all the prepared powders.

The properties of the sintered pellets are presented in Table 2. All materials were efficiently densified during the thermal treatment at 1600 °C under reducing atmosphere, with geometric densification rate over 95%, except for the heterogeneous mixed oxide that reached a densification rate of 88%. It was assumed that the sintering capability was hindered by the heterogeneous microstructure and chemical composition of this sample. To display more information during the sintering step, a dilatometry study is presented in the supplementary information (Supplementary Fig. 1). Average grain sizes were comparable and within the range of 5–10 µm.

XRD patterns of the ground sintered pellets and subsequent calculated unit cell parameters are presented in Fig. 1 and compared to that reported in literature. All the materials were found to crystallize with the fluorite-type structure ($Fm\bar{3}m$). When considering mixed oxides, peaks positions shifted to higher angles when increasing Ce content, which indicated a lattice contraction (ionic radii of U(IV) and Ce(IV) for CN = 8 equal to 1.00 Å and 0.97 Å, respectively)[44]. Moreover, these results confirmed the formation of a single solid solution in the case of the homogeneous materials. However, XRD analyses showed no evidence that the heterogeneous material consisted in a two-phase system. Lattice parameter values determined for powders heated at 700 °C were found to be lower than that expected for stoichiometric $U_{1-x}Ce_xO_2$ and did not follow the Vegard's law. This was attributed to the formation of hyper stoichiometric oxides $U_{1-x}Ce_xO_{2+\delta}$ due to the low temperature of conversion and to the high surface area of the prepared oxide powder. However, after the sintering step, all the final pellets turned out to be stoichiometric. Lattice parameters values followed the Vegard's law and were in good agreement with the values found in the literature for stoichiometric U(IV), Ce(IV) solid-solutions.

Normalized and fitted Raman spectra recorded on pristine sintered pellets are displayed in Fig. 2. Pure CeO_2 spectrum was characterized by the presence of the single T_{2g} band at ≈ 465 cm^{-1}[45]. In the case of pure UO_2, apart from the T_{2g} at 445 cm^{-1}, a large band was found at ≈ 1150 cm^{-1}, which was attributed to the 2LO mode (phonon overtone)[46,47]. No weak band was observed at ≈ 575 cm^{-1} or at 620–630 cm^{-1}, which are often assigned to the LO mode (lattice distortion) and cuboctahedral clusters formation due to further oxidation to U_4O_9, respectively[48]. This result was consistent with XRD results, confirming the stoichiometric nature of the UO_2 prepared after sintering.

When considering mixed oxides Raman spectra, three features were observed at ≈ 535 cm^{-1}, ≈ 570 cm^{-1} and ≈ 1070 cm^{-1} in addition to the T_{2g} and 2LO bands. In all cases, a single peak contribution was noted for the T_{2g} band, which indicated that it followed a single-mode vibration. This was in good agreement with the literature concerning heavy metals dioxide solid

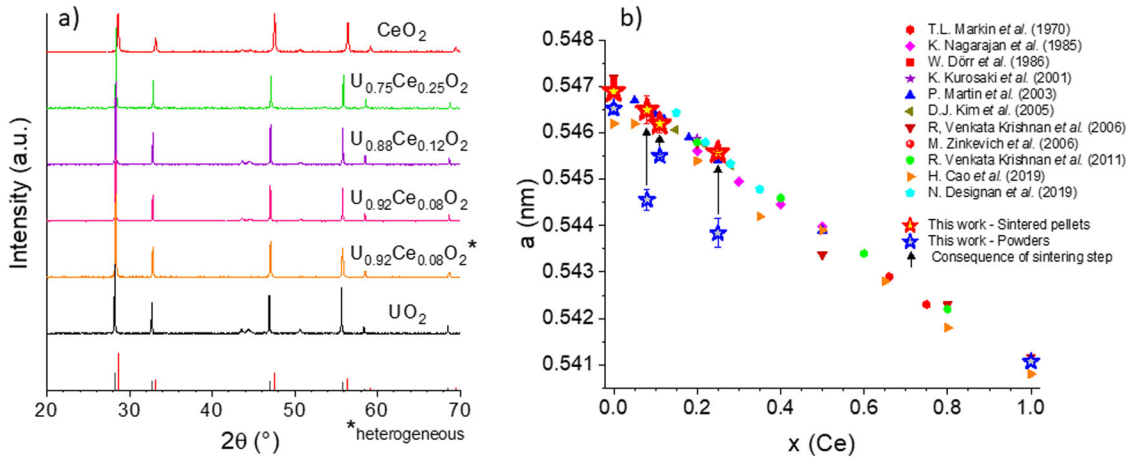

Fig. 1 XRD patterns and lattice parameters. a XRD patterns of ground pellets sintered at 1600 °C under Ar/H_2 atmosphere compared to the references UO_2 [PDF-00-041-1422] (black vertical lines) and CeO_2 [PDF-03-065-5923] (red vertical lines). **b** Lattice parameter values obtained from XRD patterns refinement of raw powders and ground sintered pellets compared to data reported in the literature. Error bars are twice the standard deviation.

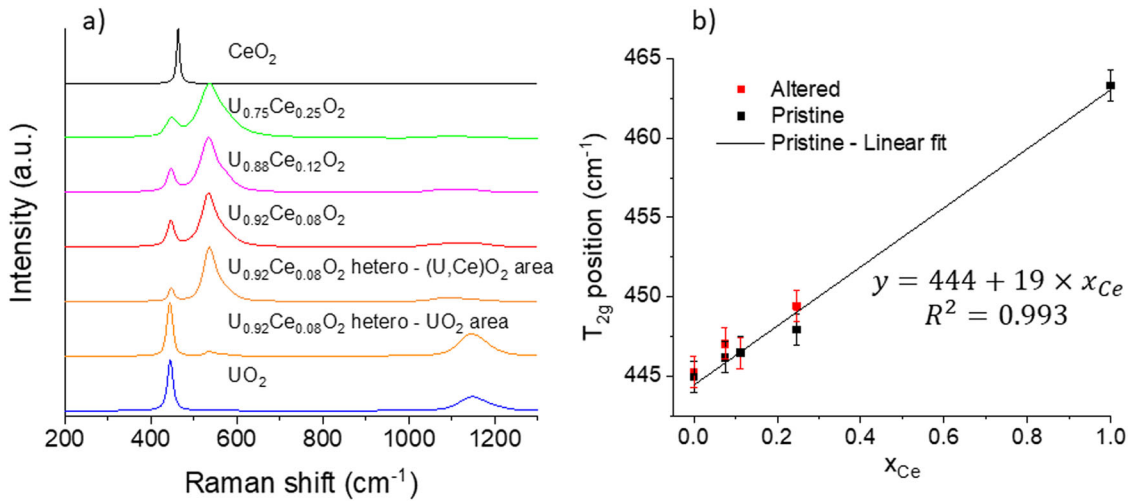

Fig. 2 Raman spectra of the prepared samples. a RAMAN spectra of pure UO_2, CeO_2 and $U_{1-x}Ce_xO_2$ pristine pellets. For the heterogeneous material: UO_2 area and $(U,Ce)O_2$ area correspond to the spectra of UO_2 dilution phase and Ce-rich agglomerates, respectively. **b** Position of the T_{2g} band of the $U_{1-x}Ce_xO_{2\pm\delta}$ as a function of Ce content before and after leaching. The black line represents the linear fit for T_{2g} position of pristine samples. Error bars correspond to the spectral resolution.

solutions[49,50]. Compare to UO_2, Elorrieta et al.[51] also observed a remarkable additional feature in their $(U,Ce)O_{2-y}$ mixed oxides spectra around 500–600 cm^{-1}, which increased in intensity with increasing Ce content. This additional feature was decomposed in two contributions. By analogy with $(M^{IV},M^{III})O_{2-y}$ mixed oxides, Elorrieta et al. associated the band observed around 530–540 cm^{-1} in the $(U, Ce)O_{2-y}$ mixed oxides spectra with the presence of oxygen vacancies that would confirm the presence of Ce(III), whereas the contribution at ~575 cm^{-1} was assigned to the LO mode. Indeed, similar features were observed by Desgranges et al.[52] in the Raman spectrum of $(U,Nd)O_{2-y}$. They interpreted the band at 570 cm^{-1} as a UO_2 Raman-forbidden mode that became active because of lower symmetry and the peak at 530 cm^{-1} as a local phonon mode associated with oxygen-vacancy-induced lattice distortion. Le Guellec et al.[53] also observed an additional band at ~575 cm^{-1} in Raman spectra of $U_{0.89}Pu_{0.11}O_2$ material. Similar features were also described by Medyk et al.[54] for $(U,Pu)O_2$ solid solutions with various plutonium contents. This band was attributed to the T_{1u} LO vibration mode, which is theoretically forbidden for the $Fm\bar{3}m$ symmetry and is thus related to the presence of structural defects distorting the local symmetry.

In the particular case of the heterogeneous material, two kinds of spectra were displayed, the first one was characteristic of UO_2 and the second one was characteristic of the Ce-rich agglomerates. Raman spectrum obtained in UO_2 area was similar to the one obtained for pure UO_2, excepted for a weak band at 535 cm^{-1}, assigned to the mixed oxide. This was due to the diffusion of cerium from Ce-rich agglomerates to the diluting UO_2 phase during the sintering step, or to the presence of $(U,Ce)O_2$ grains in the vicinity of the analyzed area. The spectra of $(U,Ce)O_2$ area was exactly the same as the one obtained for homogeneous samples.

The variation of the T_{2g} band position as a function of Ce content for the homogeneous materials was quantitatively analyzed and plotted in Fig. 2. When increasing the Ce content, the position of the T_{2g} band shifted toward higher wavenumber values. The variation of the T_{2g} band position versus the Ce content was found to be linear in the whole studied range. This result was found to be in agreement with the variation of the mixed oxides lattice parameter with the Ce content (Fig. 1) and

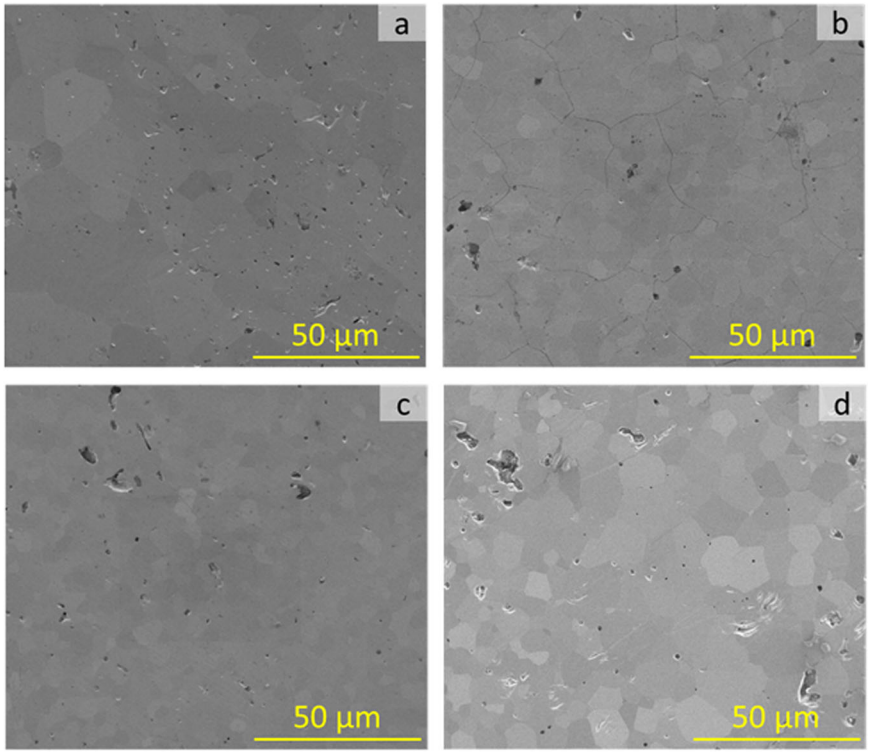

Fig. 3 SEM observation of homogeneous materials before alteration. SEM micrographs of polished pellets of homogeneous materials (SE mode) before leaching: **a** UO_2; **b** $U_{0.92}Ce_{0.08}O_2$; **c** $U_{0.88}Ce_{0.12}O_2$; **d** $U_{0.75}Ce_{0.25}O_2$.

thus, confirmed the stoichiometric nature of the mixed oxides samples after the sintering step. Nevertheless, this result appeared in contradiction with the appearance of the additional bands observed at ≈ 535 cm^{-1} and ≈ 570 cm^{-1}, which was associated in the literature with the presence of Ce(III) and oxygen vacancies. One possibility would be that the incorporation of Ce(III) was not associated with oxygen vacancies but with U(V) in the solid-solution making the attribution to the additional band in uranium-cerium mixed oxides spectra more complex.

Polished sintered pellets SEM images in SE mode are displayed for homogeneous materials in Fig. 3. The obtained microstructures were highly comparable confirming similar densification rates. Very few open pores are visible, supporting the use of the geometric surface area (ranging from 2.0 to 2.5×10^{-5} m^2, depending on the pellets size) to normalize leaching rate values.

Energy dispersive spectroscopy (EDS) performed on heterogeneous $U_{0.92}Ce_{0.08}O_2$ material is displayed in Fig. 4. Two different types of area were identified on the BSE images. The first area consisted in small grains of roughly 1 µm whereas the second area consisted in larger grains up to 15 µm. Apart from the grain size, the EDS maps showed that these areas differed by their cationic distribution. It appeared that small grains had very few cerium loading (less than 1 at. %) and thus was attributed to diluting UO_2. On the other hand, large grains area contained larger cerium loadings (in the range of 12–15 at. %). They were associated to Ce-rich agglomerates coming from the master blend. Although EDS analysis confirmed the heterogeneous cationic distribution of this material, Ce content in the Ce-rich agglomerates was found lower than the 25 at. % of the master blend. Very similar microstructure was obtained by Le Guellec et al.[53] for $U_{0.89}Pu_{0.11}O_2$ sintered pellets. They also observed small grains clusters at the pellet surface that were clearly depleted in Pu compared to the surrounding large grained polycrystalline matrix.

XPS analyses of the homogeneous $U_{1-x}Ce_xO_{2\pm\delta}$ materials (with $x = 0$, 0.08, 0.12, 0.25) were performed before the leaching experiment. Pure CeO_2 sintered pellet was also characterized by XPS and used as a reference material (Supplementary Fig. 2). XPS analysis allowed characterizing a thin layer of material at the sample surface, which is interesting to investigate when considering that alteration phenomena occur at the solid/ solution interface. The peaks area of the U 4 f and Ce 3d XPS spectra were determined to evaluate the relative atomic percentages of U(IV), U(V), Ce(III) and Ce(IV) (Table 3). Then, the percentages of the valence states of the cations obtained by XPS were used to determine the O/M ratio in the mixed oxides assuming the charge neutrality. From these results, it appeared that the charge compensation occurred both by charge transfer between U and Ce and by varying the oxygen content at the surface of the samples. Indeed, Ce(III) was present in various proportions in all the mixed oxide samples. This proportion increased with the total Ce content. The amount of U(V) was virtually constant in $UO_{2.21}$, $U_{0.92}Ce_{0.08}O_{2.16}$ and $U_{0.88}Ce_{0.12}O_{2.15}$, then decreased markedly for $U_{0.75}Ce_{0.25}O_{1.93}$. Consequently, the O/M ratio was decreasing with the increase of the Ce content, from hyper stoichiometric to hypo stoichiometric mixed oxides. These results also showed that the surface of the materials differed from the stoichiometric $U_{1-x}Ce_xO_2$ bulk material (as stated by XRD and Raman analyses). This property could influence the initial behavior of the samples during leaching experiments.

Surface characterization after leaching

After leaching, the samples were dried and stored in a glove box under Ar atmosphere. Surface characterizations by SEM (SE mode) after leaching of UO_2 and homogeneous mixed oxides in 0.20 $mmol.L^{-1}$ H_2O_2 solution are presented in Fig. 5. No significant change was observed during alteration for the homogeneous mixed oxides. It is important to note that the total alteration thicknesses did not exceed 23 nm for $U_{0.88}Ce_{0.12}O_2$ and 3 nm for $U_{0.75}Ce_{0.25}O_2$. However, UO_2 exhibited a surface entirely covered with needle-like crystals with a size inferior to 1 µm. This neoformed secondary phase was suspected to be studtite, formed

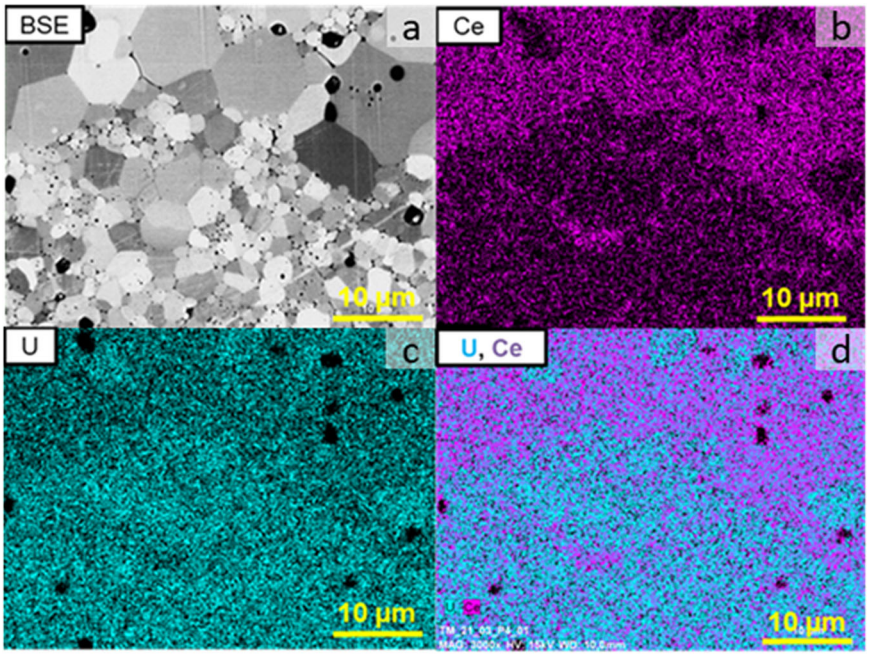

Fig. 4 SEM observations of heterogeneous material before alteration. Elemental maps of the heterogeneous $U_{0.92}Ce_{0.08}O_2$ material, **a** BSE mode; **b** Ce map; **c** U map; **d** U and Ce map.

Table 3. Results obtained from XPS analyses performed on homogeneous materials.

x_{Ce}	U(IV)		U(V)		Ce(IV)		Ce(III)		O/(U + Ce)
	at. %	$x_{U(IV)}$	at. %	$x_{U(V)}$	at. %	$x_{Ce(IV)}$	at. %	$x_{Ce(III)}$	
0	58	0.58	42	0.42			0	0	2.21
0.075	61	0.561	39	0.359	40	0.032	60	0.048	2.16
0.111	58	0.516	42	0.373	36	0.040	64	0.071	2.15
0.248	92	0.692	8	0.060	19	0.047	81	0.201	1.93
1					100	1	0	0	2.00

Atomic fractions of U(IV) and U(V) with respect to U_{tot}. Atomic fractions of Ce(III) and Ce(IV) with respect to Ce_{tot}. Corresponding stoichiometries in the solid solution.

by the chemical reaction between H_2O_2 and uranyl UO_2^{2+}, as the solution was over-saturated with respect to studtite (Supplementary Fig. 3).

SEM micrographs (SE mode) of the heterogeneous $U_{0.75}Ce_{0.25}O_2$ material are shown in Fig. 6. These images evidenced that the two types of areas, UO_2 and (U,Ce)O_2, behave differently during the leaching experiments. Large grains were still visible, and crystals with a needle-like morphology covered large surface areas up to 100 µm^2 at the surface of the pellet. These crystals were similar to that found at the surface of UO_2 pellet. Large grains were previously (Fig. 4) attributed to the Ce-rich agglomerates within the heterogeneous material. As only these grains were visible after the precipitation of the secondary phase, it was assumed that this phase precipitated only on UO_2 areas. On the other hand, Ce-rich agglomerates displayed the same behavior as found for the homogeneous mixed oxides. In other words, it did not underline any alteration features.

Raman spectra are presented in Fig. 7 for raw and leached pellets. In the case of altered UO_2 and UO_2 areas in the heterogeneous material, metastudtite was easily identified by its characteristics bands at ≈ 829 cm^{-1} and ≈ 868 cm^{-1}, attributed to the symmetric stretching vibration (v_1) of the uranyl bond (U = O) and to the stretching of the oxygen peroxide bond (O-O), respectively[55]. It is believed that metastudtite could have been formed by dehydration of studtite during analyses by SEM or Raman spectroscopy (e.g. high vacuum, heat induced by laser/electron beam). Indeed, Colmenero et al.,[56] observed the phase transition between studtite and metastudtite under air by Raman spectroscopy at low temperature (i.e. 33 °C). However, under a film of water, studtite was found to be stable up to 90 °C. This result indicated that studtite precipitated at the sample surface during the leaching experiment, then dehydrated during the analyses of the samples by SEM and Raman. A uranyl U = O bond length $d_{U=O}$ of 178.2 ± 0.1 pm was determined using the expression derived by Bartlett and Cooney[57] as follows:

$$d_{U=O}(\mathrm{pm}) = 10650 \times v_1^{-2/3} + 57.5 \quad (1)$$

This value is in good agreement with the length of a uranyl bond found in studtite or meta-studtite reported in literature (i.e. 177.9 ± 0.3 and 177.3 ± 0.3 pm, respectively)[58].

As for the homogeneous mixed oxides materials and the (U,Ce)O_2 areas in the heterogeneous material, Raman spectra did not exhibit additional bands after leaching. However, one can notice that the position of the T_{2g} band of altered samples shifted toward higher wavenumbers, suggesting that the Ce content slightly increased (Fig. 2). In addition, the relative intensity of the T_{2g} band with respect to the ≈ 535 cm^{-1} band decreased (especially for $U_{0.75}Ce_{0.25}O_2$ and $U_{0.88}Ce_{0.12}O_2$) and the LO band contribution at ≈ 570 cm^{-1} decreased. All these findings strongly suggested a cerium enrichment at the surface of the pellet during the leaching experiment.

Analyses of the leachates

The evolution of the U elemental concentration during the leaching of the homogeneous materials is shown in Fig. 8. An initial pulse characterized by a high elemental concentration of uranium in solution was observed for every leaching test. Then, a steady state was reached after 250–370 hours of dynamic leaching. U elemental concentration was found to be 2 to 3 orders of magnitude lower than that of the initial pulse. The

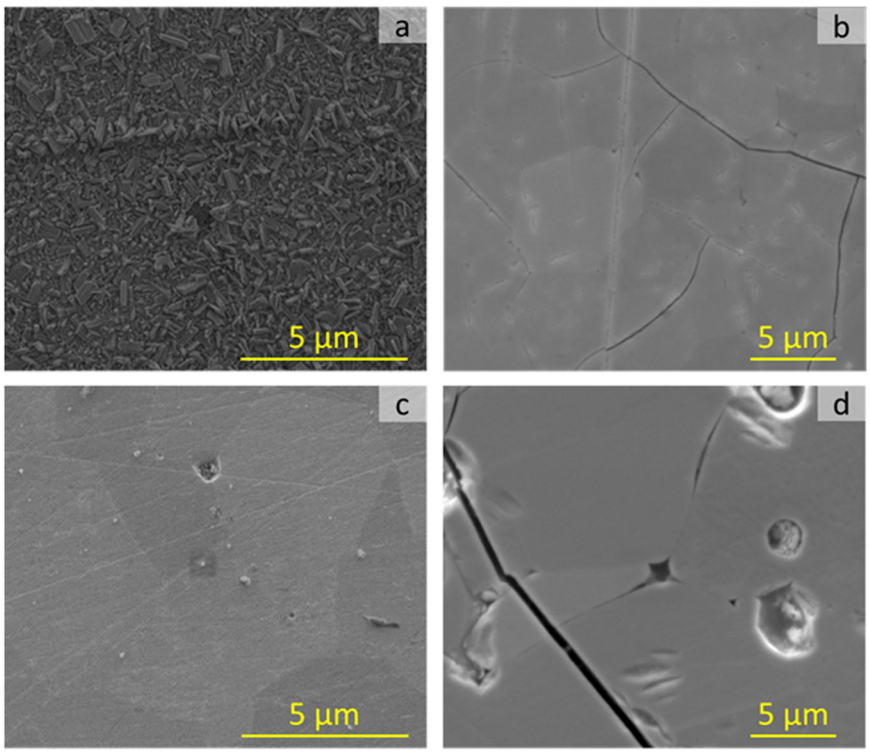

Fig. 5 SEM observations of homogeneous materials after alteration. Polished sintered pellets of homogeneous materials SEM images (SE mode) after leaching in 0.20 mmol.L^{-1} H_2O_2 solution: **a** UO_2; **b** $U_{0.92}Ce_{0.08}O_2$; **c** $U_{0.88}Ce_{0.12}O_2$; **d** $U_{0.75}Ce_{0.25}O_2$.

elemental cerium concentrations in the outflow were also systematically measured and they were found to be below the detection limit of the ICP-MS (i.e. 7×10^{-11} mol.L^{-1}).

The evolution of the H_2O_2 concentration determined in both the feeding solution and the leachates during a set of experiments are displayed in Fig. 8 (similar results obtained during the leaching of UO_2, $U_{0.92}Ce_{0.08}O_2$ and $U_{0.88}Ce_{0.12}O_2$ pellet are given in Supplementary Fig. 4). Experimental concentrations were found to be close to the target value of 2×10^{-4} mol.L^{-1}, ranging between 1.5 and 2.3×10^{-4} mol.L^{-1} for all experiments. It guaranteed the comparability of the experiments and the composition stability of the feeding solution. pH values in the leachates were found to be close to the values obtained in the feeding solution, roughly in the range of 6.9–7.3. In the same manner, the redox potential, E_h, was found to be constant during all experiments, with a mean value of ≈ 460 mV/NHE, showing oxidizing conditions. Measured dissolved dioxygen content was closed to the concentration of a solution at equilibrium with air, i.e. approximately 2.6×10^{-4} mol.L^{-1}. These results are shown in the supplementary information (Supplementary Figs. 5–7) and ascertain that the experiments were comparable and that the conditions were constant during the experiments. Thus, no evolution of the chemical conditions could explain the observed changes in the U release.

The uranium elemental concentration and associated saturation index with respect to studtite as well as the total alteration thickness at the end of the initial pulse (t = 50 h) are shown in Fig. 9. The U elemental concentration at the pulse was found to be lower when increasing the cerium content in the material, with a maximum of ≈ 10^{-6} mol.L^{-1} for pure UO_2 and a minimum of 5×10^{-9} mol.L^{-1} for $U_{0.75}Ce_{0.25}O_2$ (Table 4). This result implied that the presence of cerium inhibited the initial uranium release. Besides, the total alteration thickness at the end of the pulse was excessively low, ranging from 2 to 50 nm. This result indicated that this initial stage involved the very thin layer of material at the sample surface, which was characterized by XPS. The heterogeneous material showed an intermediate behavior between UO_2 and homogeneous $U_{0.92}Ce_{0.08}O_2$, certainly due to the high surface area of UO_2-type zones at the surface of the pellet.

The elemental uranium concentrations obtained from leachate analyses at steady state are summarized in Table 4. At steady state, for homogeneous mixed oxide samples, the same trend is observed as for the initial pulse, uranium concentrations tend to be lower when increasing the cerium content. However, UO_2 did not follow the same trend as its uranium elemental concentration at steady state was as low as the one determined for the homogeneous $U_{0.75}Ce_{0.25}O_2$. Although the result obtained for the heterogeneous material was shown in this table, the steady state was not achieved as the concentration was still decreasing. In this case, the concentration value reported in Table 4 was the last value measured. The normalized steady state alteration rate R_{ss} was calculated for all materials. As the precipitation of metastudtite was not observed at the surface of the homogeneous mixed oxide samples, R_{ss} was equal to the normalized dissolution rate, R_L. For homogeneous materials, the normalized dissolution rate was found to decrease with the Ce content.

Normalized leaching rates determined at the steady state (R_{ss}) according to elemental uranium concentration in the leachates are presented in Fig. 10 for all the homogeneous materials. Due to the precipitation of studtite, the R_{ss} values estimated for UO_2 and for the heterogeneous sample (i.e. 0.9 mg.m^{-2}.d^{-1} and 3.2 mg.m^{-2}.d^{-1}, respectively) were not directly comparable with dissolution rate values obtained for the homogeneous $U_{1-x}Ce_xO_2$ solid solutions and with the data found in literature. Thus, these results are not displayed in Fig. 10. For all the homogeneous materials, the uranium release in solution was not affected by the possible precipitation of neoformed phase. Therefore, the obtained values of the normalized leaching rate can be compared with data from the literature in similar conditions. Although there is no data available for the mixed oxides $(U,Ce)O_2$, many studies were carried out with UO_2. Normalized dissolution rates of UO_2

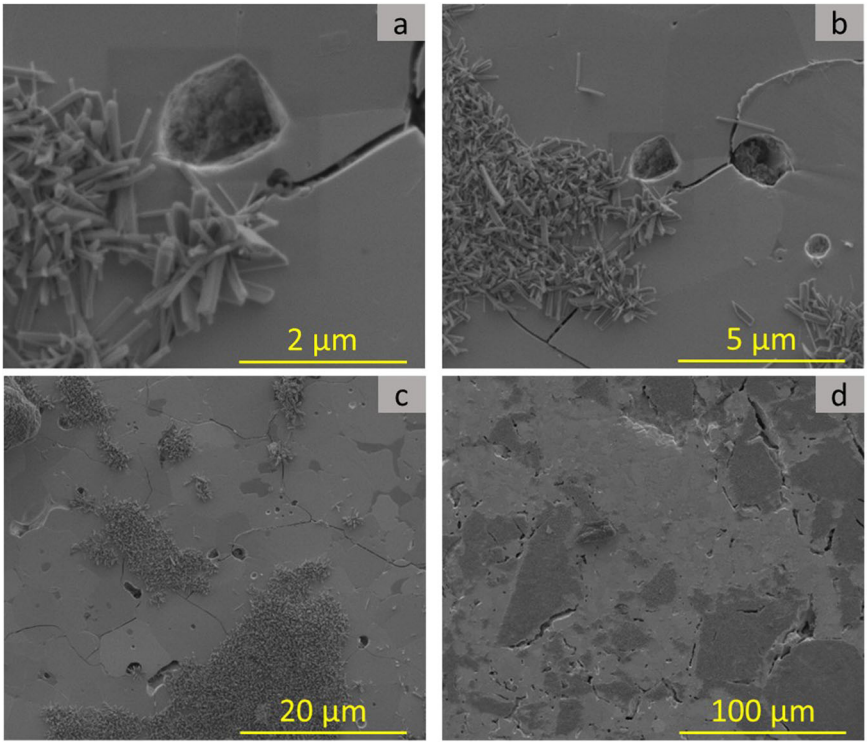

Fig. 6 SEM observations of heterogeneous material after alteration. SEM images (SE mode) of heterogeneous $U_{0.92}Ce_{0.08}O_2$ material after leaching in 0.20 mmol.L^{-1} H_2O_2 solution at different magnifications **a** ×25,000; **b** ×10,000; **c** ×2500; **d** ×500.

obtained in the presence of H_2O_2 were found to vary on a range up to 2 orders of magnitude depending on the authors. It is important to note that many parameters can affect this value, such as the concentrations of hydrogen peroxide and carbonate ions, pH, E_h, ionic strength or the presence of dissolved dioxygen. A study carried out by Casas et al.[59] dedicated to the leaching of UO_2 powder in water containing 10^{-4} mol.L^{-1} H_2O_2 under dynamic conditions yielded a normalized dissolution rate of 22.6 mg.m^{-2}.d^{-1}. Despite a H_2O_2 concentration two times lower than in the present work, this dissolution rate is already 6 to 7 times higher than the one obtained for the $U_{0.92}Ce_{0.08}O_2$ homogeneous material (Table 4). Nevertheless, carbonate ions concentration was 20 times higher than that used in the present work, which can facilitate the solubilization of U(VI) produced at the surface of UO_2 by complexation with U(IV) at the solid/solution interface.

A multi-parametric study carried out by De Pablo et al.[60] in both dioxygen-free and carbonate-free aqueous solution at pH = 6 highlighted a linear increase of the logarithm of the normalized dissolution rate of UO_2 with the concentration of H_2O_2. Even though the validity domain of the experimental expression derived by De Pablo et al. (Eq. 2) is limited to H_2O_2 concentration below 10^{-4} mol.L^{-1} and pH = 6, the experimental conditions were close enough to our conditions to be used as a comparison:

$$\log R_L = -(5.8 \pm 0.2) + (0.93 \pm 0.04) \times \log[H_2O_2] \quad (2)$$

where R_L is expressed in mol.m^{-2}.s^{-1} and $[H_2O_2]$ is expressed in mol.L^{-1}.

The calculated value of R_L using this expression in our conditions yielded a normalized dissolution rate of 11.9 mg.m^{-2}.d^{-1} and was, as for Casas et al.,[59] higher than the values determined in this work for $U_{0.92}Ce_{0.08}O_2$ homogeneous material. Under similar conditions than that used by De Pablo et al.,[60] but using dynamic leaching, Clarens et al.[8] determined a normalized dissolution rate of 8.8 mg.m^{-2}.d^{-1} for a H_2O_2 concentration of 10^{-4} mol.L^{-1} that was half of that used in the present work. These values obtained from literature were of the same order of magnitude than that obtained in this study but were all higher. It could be argued that the precipitation of studtite lowered the apparent leaching rate. Nevertheless, according to the linear regression of the normalized dissolution rates values calculated for the homogeneous $U_{1-x}Ce_xO_2$ materials in Fig. 10, we would expect by extrapolation to $x_{Ce} = 0$ a value close to 5 mg.m^{-2}.d^{-1} for UO_2, which was still lower than the values estimated from the literature. This supported the idea that solid solutions of $U_{1-x}Ce_xO_2$ did not behave as UO_2 during leaching in the presence of H_2O_2 and that the cerium inhibited the uranium release. Moreover, this assumption also supported the trend observed for the elemental uranium concentration measured in the leachates during the initial pulse.

To gain insights into our understanding of the role of Ce in H_2O_2 decomposition and studtite precipitation at the surface of pellets, additional static leaching experiments were performed. The composition of the solution in contact with the pellets was similar to the one used in dynamic experiments, except that oversaturated conditions with respect to studtite were imposed initially by adding uranyl nitrate to the reactors ($[U] = 1.6 \times 10^{-7}$ mol.L^{-1}). Each reactor contained two pellets submitted to the same alteration scenario ($UO_2 + CeO_2$ and $UO_2 + U_{0.92}Ce_{0.08}O_2$). The evolution of the uranium and H_2O_2 concentrations determined in the reactors and in the blank experiment are showed in Fig. 11. The obtained results showed the decrease of the uranium concentration in the three reactors at different rates. In parallel, the hydrogen peroxide concentration was found to decrease only significantly in the reactors containing pellets. Considering the magnitude of the decreases of the U and H_2O_2 concentrations, the precipitation of studtite could not explain by itself the decrease of the H_2O_2 concentration. Thus, the presence of the pellets increased the rate of hydrogen peroxide decomposition. At the end of experiments, the surface of the four pellets were observed by ESEM. Figure 11 shows representative micrographs of the surface of UO_2, $U_{0.92}Ce_{0.08}O_2$

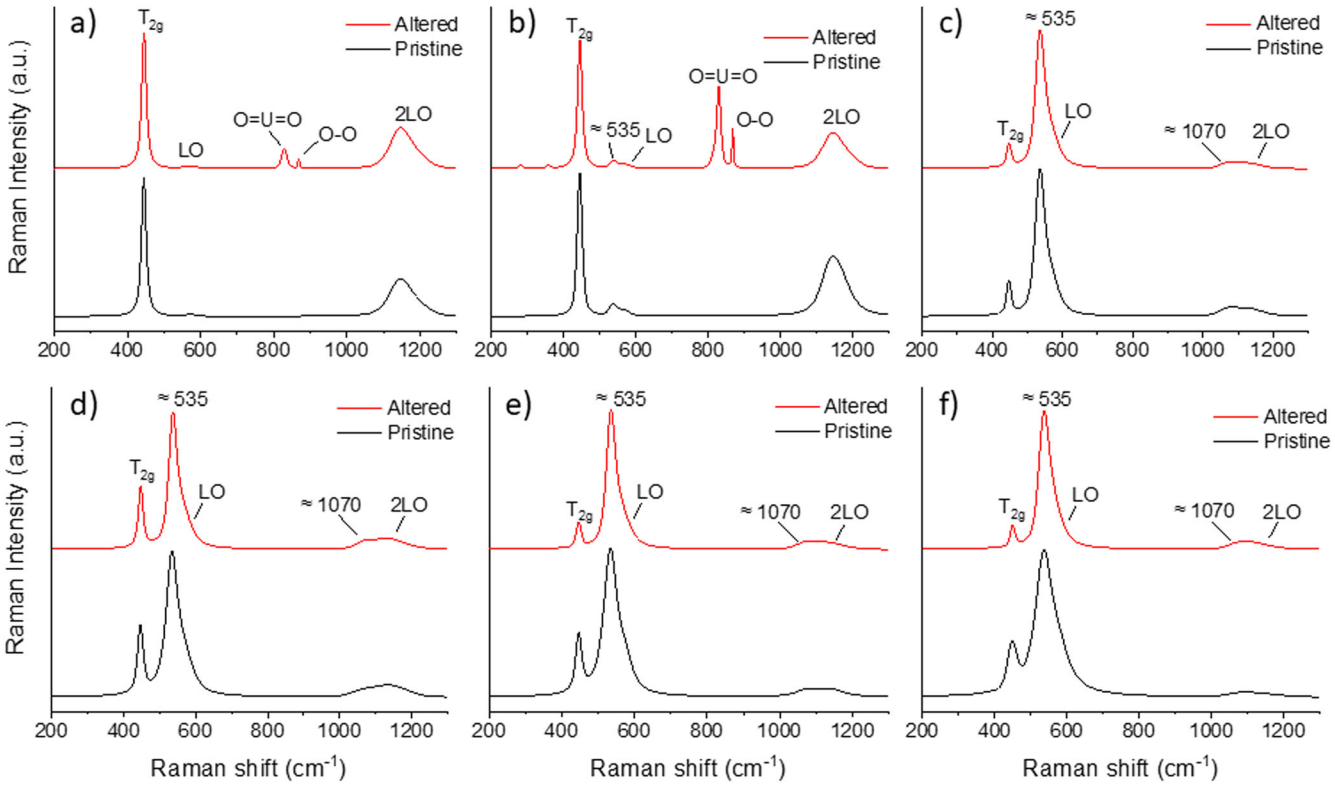

Fig. 7 Raman spectra of altered samples. Raman spectra before and after leaching in 0.20 mmol.L^{-1} H_2O_2 solution of **a** UO_2; **b** heterogeneous material – UO_2 area; **c** heterogeneous material – $(U,Ce)O_2$ area; **d** $U_{0.92}Ce_{0.08}O_2$; **e** $U_{0.88}Ce_{0.12}O_2$; **f** $U_{0.75}Ce_{0.25}O_2$.

and CeO_2 pellets. These observations revealed that the surface of UO_2 pellets was entirely covered by neoformed crystals, whereas only few crystals were evidenced at the surface of $U_{0.92}Ce_{0.08}O_2$ pellet. Moreover, virtually no crystal was detected at the surface of CeO_2. These experiments demonstrated that the precipitation of studtite was located at the surface of the UO_2 grains and that the presence of Ce inhibited the formation of this phase at the solid/solution interface. This result strengthened the idea of catalytic decomposition of H_2O_2 by Ce at the surface of $U_{1-x}Ce_xO_2$ solid solutions.

DISCUSSION

The leaching rate determined from the uranium concentration at steady state for homogeneous $U_{1-x}Ce_xO_2$ solid solutions was found to decrease with the Ce content in the material (Table 4). The precipitation of studtite was never observed at the surface of homogeneous mixed oxide samples, potentially as the consequence of the decrease of the saturation index with respect to this phase. Contrary to that observed for UO_2 and heterogeneous $U_{0.92}Ce_{0.08}O_2$ samples, this phenomenon was not responsible for the decrease of the leaching rate. Moreover, it is worth noting that the elemental cerium concentrations in the outflow were below the detection limit of the ICP-MS (i.e. 7×10^{-11} mol.L^{-1}). From U concentration measured at steady state, and assuming a congruent dissolution for $U_{0.75}Ce_{0.25}O_2$ mixed oxides, the elemental cerium concentration should be equal to 1.7×10^{-10} mol.L^{-1}. This value was still above, but close to the detection limit of the analytical method, so it was difficult to assert that Ce was not released in solution during the leaching experiment. Nevertheless, the decrease of the leaching rate of the $U_{1-x}Ce_xO_2$ solid solutions was undoubtedly related to the presence of Ce. Three main hypotheses could explain this behavior. First, the formation of a thin layer composed of Ce oxide or hydroxide exhibiting low solubility[61] could induce passivation of the surface of the homogeneous mixed oxides samples. Second, the presence of Ce could favor the catalytic decomposition of H_2O_2[62] and thus reduce the activity of this species at the sample surface. Third, the incorporation of Ce(IV) in the fluorite structure of UO_2 could improve its durability against oxidative species.

The presence of a secondary phase at the sample surface was not evidenced neither by ESEM nor by Raman spectroscopy. However, if this latter existed, the thickness of this Ce enriched layer might prevent its detection by these techniques. The phase stability diagram of Ce(III/IV) in aqueous systems containing or not H_2O_2 was investigated in a series of papers[63–65]. Analysis of the Pourbaix diagram established by Yu et al.[63] showed that the pH and E_h values maintained during the dynamic leaching experiments (i.e. 6.9 to 7.3 and 0.46 V/NHE, respectively) fell in the $Ce(OH)_4/CeO_2{\cdot}xH_2O$ stability domain. Thus, these phases were the most likely Ce(IV) precipitates. Hayes et al.[65] listed the values reported in the literature for the standard Gibbs free energy of formation of CeO_2. $\Delta_fG°(CeO_2, 298.15\ K)$ was ranging between −1025.33 and −986.04 kJ.mol^{-1}. Using these data and $\Delta_fG°(Ce^{4+}, 298.15\ K) = -503.8$ kJ.mol^{-1}, the log $K_s°$ of the following dissolution reaction was evaluated:

$$CeO_2(s) + 4H^+(aq) \rightleftarrows Ce^{4+}(aq) + 2H_2O \quad (3)$$

The calculated log $K_s°$ varied between −8.28 and −1.39. A solubility constant for CeO_2 is also given in the Lawrence Livermore National Laboratory thermodynamic database, LLNL-TDB[66] (i.e. log $K_s°(CeO_2, 298.15\ K) = -8.16$). Actually, the log $K_s°$ $(CeO_2, 298.15\ K)$ reported in the literature are associated either to crystalline or to freshly precipitated CeO_2, which can explain the high variability of the obtained values. The solubility of Ce in a 1.6×10^{-4} mol.L^{-1} $NaHCO_3$ solution with pH = 7 and $E_h = 460$ mV/NHE (i.e. similar to the one used in the leaching experiments), was calculated using different solubility constants (log $K_s°(CeO_2,$

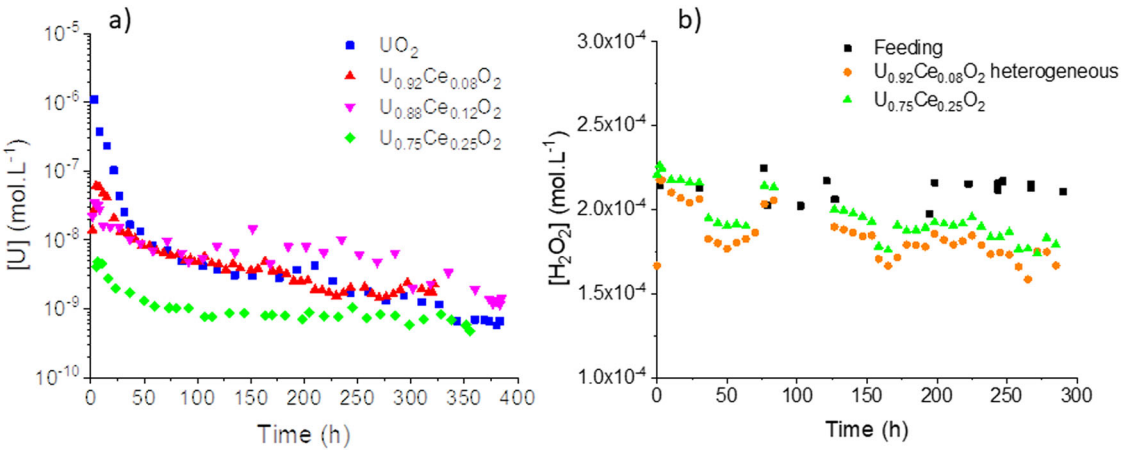

Fig. 8 Evolution of concentrations during dynamic experiments. a Evolution of U elemental concentration during the leaching of homogeneous materials in a solution containing 0.20 mmol.L^{-1} of H_2O_2, 0.16 mmol.L^{-1} of HCO_3^- at pH = 7.0 ± 0.2 and 22 °C; **b** Evolution of the concentration of H_2O_2 in the inlet and in the outlet of the reactor during the leaching experiments performed on heterogeneous $U_{0.92}Ce_{0.08}O_2$ and homogeneous $U_{0.75}Ce_{0.25}O_2$ materials. Error bars are twice the standard deviation.

298.15 K) = −8.16, or −1.39) with Phreeqc software and the LLNL-TDB. Consequently, Ce elemental concentration was found to vary between 8×10^{-15} and 4.6×10^{-8} mol.L^{-1}. The predominant species were $CeCO_3^+$ and Ce(III) with almost similar amount. These thermodynamic calculations showed that the low elemental cerium concentration monitored at the outlet of the dissolution reactor could be controlled by the precipitation of $CeO_2{\cdot}xH_2O$. This freshly precipitate could act as a passivating barrier at the pellet surface, which would explain the decrease of the leaching rate of $U_{1-x}Ce_xO_2$ solid solutions.

Several studies report the addition of hydrogen peroxide to Ce(III) solutions to depose at a fast rate Ce-based coatings on metals[67]. This deposit imparts corrosion protection to the underlying metal. For this reason, the preparation of nanocrystalline ceria by homogeneous precipitation route was extensively studied. The experimental protocol relied on the production of a precursor deposited at the metal surface by oxidation of Ce(III)(aq) with H_2O_2. This reaction produces $Ce(OH)_2^{2+}$(aq) species, which is further hydrolysed to $Ce(OH)_4$ at near neutral pH and a precipitate is formed. Then, this precursor is transformed to CeO_2(s) by thermal treatment. An alternative mechanism involves the formation of intermediate Ce(III) peroxo-complexes, then the precipitation of hydroxyl peroxo-containing Ce(IV) species, which is slowly transformed at room temperature to hydrated CeO_2(s)[67]. The presence of H_2O_2 is also known to influence the physical and chemical properties of the Ce-containing precipitates[68]. Investigations of the morphology and crystallinity of the precipitates formed at room temperature by addition of H_2O_2 to Ce(III) solutions showed that a large excess of H_2O_2 favored the formation of a mixture of nanometric particles of CeO_2 and amorphous phase. Increasing the H_2O_2/Ce molar ratio in solution leads to the decrease of the CeO_2 crystallite size and to the increase of the amount of amorphous phase. Additionally, Raman spectroscopy, XPS Ce 3d and O 1 s spectra revealed the presence of η^2-peroxide (O_2^{2-}) species coordinated to Ce(IV) in the precipitates formed at high H_2O_2 concentration. It is noteworthy that the presence of the O-O stretching vibration of (O_2^{2-}) species, observed at 834 cm^{-1} or at 842 cm^{-1} by Scholes et al.[67,68] in Ce(IV)-containing precipitates, was not identified in the Raman spectra obtained after leaching of the homogeneous $U_{1-x}Ce_xO_2$ samples (Fig. 7). In our leaching experiments, the elemental cerium concentration was several orders of magnitude lower than H_2O_2. Thus, H_2O_2 controlled the redox potential and at near-neutral pH, Ce(IV) precipitates were likely to be formed. The nature of the precipitates remained unknown and its identification requires further investigations using surface characterization techniques with high resolution in the direction normal to the sample surface. The identification of the surface precipitate is made even more complex by its similar nature with the underlying material, its low crystallinity and thickness.

In addition, nanoparticles of ceria are also extensively studied and used as catalyzers, taking advantage of the unique redox properties of CeO_{2-y} that associates Ce(III) with oxygen vacancies, and the enhanced surface reactivity of nanomaterials[69]. Especially, nanoceria provides excellent antioxidant activity in aqueous solutions and was found to enhance hydrogen peroxide disproportionation into O_2 and H_2O, as some specific enzymes do in living cells. This property is considered as a great advantage in several biological applications[70]. Seminko et al.[62] proposed recently a mechanism of H_2O_2 decomposition based on Ce(III)/Ce(IV) redox cycles. They observed oscillations of the Ce(III)/Ce(IV) ratio in ceria nanoparticles by luminescence spectroscopy associated to H_2O_2 decomposition at near neutral pH. They also observed that the rate of H_2O_2 decomposition increased when decreasing the size of the ceria nanoparticles. This mechanism, based on redox cycles, does not necessarily require the solubilization of Ce(IV) species, but occurs at the surface of CeO_{2-y} nanoparticles. According to the Pourbaix diagram of the Ce(III/IV)-H_2O-H_2O_2/O_2 system[63], at the E_h and pH values maintained during the leaching experiments (i.e. E_h = 0.46 V/NHE and pH = 7), Ce(IV) can oxidize H_2O_2 leading to the formation of Ce(III) and molecular O_2. Then, Ce(III) species can reduce H_2O_2 into H_2O, being oxidized back into Ce(IV). It remained unclear if H_2O_2 decomposition could occur through a similar mechanism at the surface of $U_{1-x}Ce_xO_2$ samples without any solubilization of Ce, or due to the formation of a secondary Ce(IV)-containing phase that exhibits similar properties as CeO_{2-y} nanoparticles. In both cases, the activity of H_2O_2 at the sample surface should decrease leading to the inhibition of the oxidative dissolution and to the decrease of the apparent leaching rate of the mixed oxide. Although the bulk solution was supersaturated with respect to studtite, the precipitation of this phase was neither observed at the surface of the $U_{1-x}Ce_xO_2$ solid solutions, nor at the surface of the mixed oxide grains in the heterogeneous sample (Fig. 6). The static experiments also confirmed this observation for pellets submitted exactly to the same alteration scenario, massive precipitation of studtite was only observed at the surface of UO_2, whereas the H_2O_2 concentration in the bulk solution was strongly decreasing in all experiments involving Ce-containing pellets. This observation was a strong indication that undersaturated conditions were

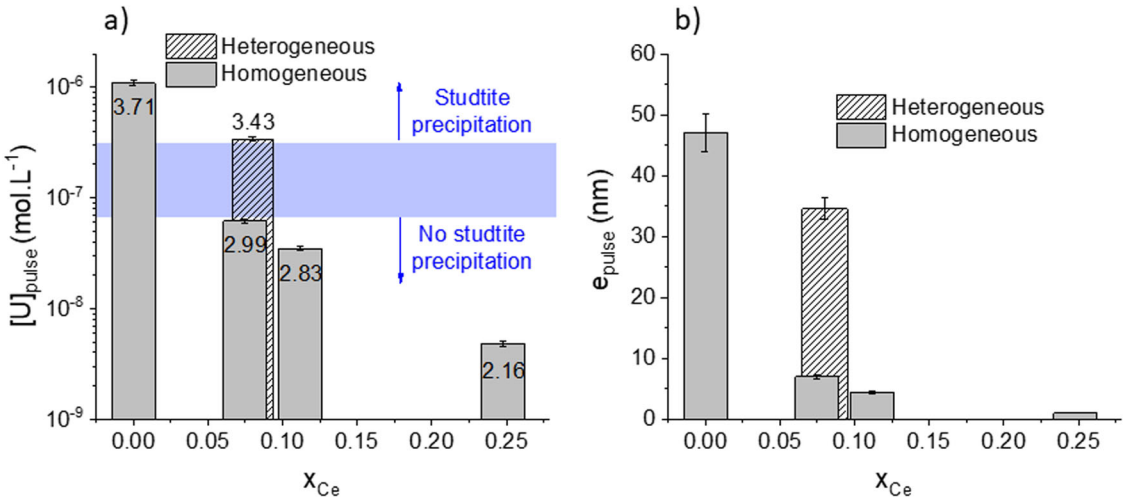

Fig. 9 Comparison of leaching experiments. a Elemental uranium concentration in the leachate as a function of the Ce content during the initial pulse – Saturation index with respect to studtite is indicated for each case. The dotted blue lines indicate the presence (upper line) and the absence (bottom line) of metastudtite observation at the samples surface. **b** Total alteration thickness at the end of the pulse (t = 50 h) as a function of the Ce content. Error bars are twice the standard deviation.

maintained near surface of U_{1-x} Ce_xO_2 solid solutions and that it could be caused by the decomposition of H_2O_2.

Finally, the presence of Ce incorporated in the UO_2 matrix can affect the oxidation state of uranium in the $U_{1-x}Ce_xO_{2\pm y}$ solid solution. It is well known that the chemical properties of uranium, especially its solubility, depend strongly on its valence state. Thus, any factor that inhibits or catalyzes uranium oxidation step at the solid/solution interface is expected to exhibit a similar influence on the rate of UO_2 dissolution. The incorporation of trivalent elements in the fluorite structure of UO_2, like Gd(III), confers to the UO_2 doped material an increasing resistance to oxidation[71] and an increasing chemical durability against oxidative dissolution[72]. Casella et al.[72] obtained significantly lower dissolution rates for UO_2 doped with less than 4 wt.% of gadolinium in carbonated solutions at various O_2(aq) concentrations and temperatures. At elevated temperatures, the dissolution rate of pure UO_2 sample doped with the highest Gd fraction was found to be two orders of magnitude lower than that of pure UO_2. This strong effect was explained in the literature[73] by a net negative charge of the $U_{1-x}Gd_xO_{2\pm y}$ material. Indeed, if the defect of positive charge introduced by Gd(III) cations is not fully compensated by the presence of U(V), and assuming that oxygen vacancies are not created, this global negative charge repels interstitial oxygen ions. If oxygen vacancies are formed to partially compensate the deficit in positive charge, these vacancies would be first occupied by oxygen ions and it can be assumed that this effect may also delay oxidation of the matrix uranium from the (IV) to the (VI) valence state. Thorium (IV) is the only stable oxidation state in the $U_xTh_{1-x}O_2$ solid solution. Therefore, only uranium can change its oxidation state in this system. Nevertheless, it is widely admitted that the incorporation of thorium in UO_2 matrix increases also the chemical durability of the material, either in conditions representative of the geological disposal of spent nuclear fuel[74–76] or in more acidic and oxidizing media[77–79]. The higher the Th content, the lower is the dissolution rate. Thus, the enhanced chemical durability of the $U_xTh_{1-x}O_2$ solid solution was associated to the decrease of the number of oxygen interstitial sites in the vicinity of uranium atoms. Contrarily to Gd and Th, Ce can adopt both (III) and (IV) valence states, which makes the system even more complex. DFT studies[80] and experimental XPS investigations of $U_{1-x}Ce_xO_{2\pm y}$ solid solutions[81–83] showed a complex dependence of the U and Ce valence states. The presence of U(V) and Ce(III) in the solid solution results from the charge transfer between U(IV) and Ce(IV). The mixing energy model proposed by Hanken et al.[80] predicted that the atomic fraction of Ce(III) in a stable mixed-charge solid solution depends strongly on the temperature and the total Ce content. At room temperature and for $x_{Ce} \leq 0.25$, this fraction should be less than 5 at. %. This estimation was much lower than the results generally obtained by XPS, including ours (Table 3), but Hanken et al.[80] indicated that the equilibrium degree of charge disordering, quantified by the Ce(III) over (Ce(III) + Ce(+V)) ratio, could be significantly enhanced near the surface relative to the bulk. From XPS analyses of the pellets before leaching, it appeared that Ce(III) was present in various proportions in all the $U_{1-x}Ce_xO_{2\pm y}$ solid solutions. This proportion increased with the total content of Ce. The amount of U(V) was virtually constant in $UO_{2.21}$, $U_{0.92}Ce_{0.08}O_{2.16}$ and $U_{0.88}Ce_{0.12}O_{2.15}$, then decreased markedly for $U_{0.75}Ce_{0.25}O_{1.93}$. Consequently, the O/M ratio was decreasing with the increase of the Ce content, from hyper stoichiometric to hypo stoichiometric mixed oxides. By analogy with UO_2 doped with trivalent cations, the presence of Ce(III) in a thin surface layer could explain the decrease of the U concentration measured during the pulse at the beginning of the leaching experiment of $U_{1-x}Ce_xO_{2\pm y}$ solid solutions (Table 4, Fig. 9). It was not obvious that this thin layer was maintained at the surface of the pellet after the pulse event, and continued to inhibit or slow down the oxidation of U(IV). Indeed, XRD analysis and Raman spectroscopy showed that the underneath bulk material was composed of stoichiometric $U_{1-x}Ce_xO_2$ material. However, in that case, the presence of Ce(IV) only could be sufficient to protect U(IV) against oxidation as Th did in $U_xTh_{1-x}O_2$ solid solutions[72–77]. In the event that the Ce(III)/U(V)-containing surface layer was dissolved, it could lead to the precipitation of a Ce(IV) passivating layer also decreasing the uranium leaching rate and whose properties could reduce the activity of the main oxidative species by decomposition of H_2O_2. Finally, all these mechanisms could contribute in a synergistic way to improve the resistance of the (U, Ce) mixed oxides against oxidative dissolution compared to pure UO_2.

Last but not least, the analogy of behavior between these (U,Ce) O_2 model materials and $(U,Pu)O_2$ MOX fuels appeared reasonable and satisfying from various points of view. Firstly, from a chemical point of view, the oxidative dissolution decreased with the cerium content as observed for $(U,Pu)O_2$ MOX pellets[29–31]. Kerleguer et al.[31] observed that the oxidative dissolution rate decreased considerably for a homogeneous $U_{0.73}Pu_{0.27}O_2$ MOX fuel under

Table 4. Concentrations obtained at the pulse and at the steady state, normalized alteration rate determined at the steady state, saturation index of the solution at the uranium pulse and at the steady state with respect to studtite and total alteration thickness at the end of experiment calculated using Eq. 10.

	Material	$[U]_{pulse}$ (10^{-9} mol.L^{-1})	$[U]_{steady\ state}$ (10^{-9} mol.L^{-1})	$R_{ss}(U)$ (mg.m^{-2}.d^{-1})	SI_studtite Pulse Steady state	Total alteration thickness (nm)
With precipitation	UO_2	1090 ± 5	0.65 ± 0.04	0.9 ± 0.1	3.71 1.30	51
	$U_{0.92}Ce_{0.08}O_2$ heterogeneous	340 ± 3	2.2[a]	3.2[a]	3.43 1.86	51
Without precipitation	$U_{0.92}Ce_{0.08}O_2$	61 ± 1	1.79 ± 0.09	2.8 ± 0.2	2.99 1.70	13
	$U_{0.88}Ce_{0.12}O_2$	35 ± 1	1.32 ± 0.10	2.3 ± 0.2	2.83 1.60	19
	$U_{0.25}Ce_{0.25}O_2$	5 ± 1	0.51 ± 0.04	0.9 ± 0.1	2.16 1.22	3

[a]estimation based on the last concentration value.

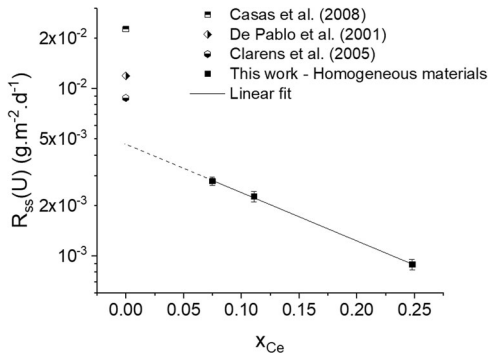

Fig. 10 Comparison of leaching rates. Normalized leaching rate R_{ss} determined for homogeneous materials as a function of the cerium content (for $[H_2O_2] = 0.20$ mmol.L^{-1}, $[HCO_3^-] = 0.16$ mmol.L^{-1}, pH = 7.0 ± 0.2 and T = 22 °C). Comparison with data reported in the literature for pure UO_2. Error bars are standard error of the mean.

alpha radiolysis of water. This slowdown was attributed to the conjunction of two effects: the enrichment of the surface in plutonium via the precipitation of a plutonium hydroxide passivating the surface, and the catalytic decomposition of the hydrogen peroxide at the surface that seemed to be favored. Indeed, these authors measured H_2O_2 concentration lower than 10^{-7} mol.L^{-1} for a homogeneous $U_{0.73}Pu_{0.27}O_2$ MOX altered in carbonated water. Such low H_2O_2 concentration was unexpected considering the alpha activity of the pellet, especially when compared to the results obtained under the same alteration conditions for heterogeneous MIMAS® MOX fuel[30]. Kerleguer et al.[31] assumed that catalytic disproportionation of H_2O_2 occurred at the surface of MOX with elevated Pu content. Several mechanisms involving either Pu(IV)/Pu(III) or Pu(V)/Pu(IV) redox couples were mentioned by the authors to describe the catalytic decomposition of H_2O_2. The results obtained in this work for Ce (which has only two stable oxidation states) indicated that the Pu(IV)/Pu(III) redox couple is most likely responsible for H_2O_2 decomposition at the surface of the pellet. Actually, the presence of cerium in the homogeneous model materials led to a different reactivity of the surface with respect to H_2O_2 compared to uranium dioxide. For an identical solution chemistry favorable to the studtite precipitation, the formation of this phase was not observed at the surface of the pellet containing cerium, which suggested the existence of catalytic decomposition of hydrogen peroxide at the solid/solution interface. Secondly, regarding the influence of the microstructure, the analogy between $(U,Ce)O_2$ heterogeneous materials and $(U,Pu)O_2$ MOX fuels was very good. Indeed the zones with low plutonium[30,84] or cerium contents (this study) dissolved preferentially and were the place of the precipitation of studtite whereas the zones with higher cerium and plutonium contents remained unchanged.

METHODS

Synthesis and sintering of materials

Various homogeneous materials $U_{1-x}Ce_xO_{2\pm\delta}$, with x values ranging from 0 to 0.25, were prepared by wet chemistry route, involving hydroxide coprecipitation[85]. A mixture containing uranium (IV) and cerium (IV) with the targeted stoichiometric ratio was promptly added to an aqueous solution consisting of a large excess of ammonia (400%) at room temperature. Uranium (IV) solution was obtained by dissolution of metallic uranium chips in concentrated hydrochloric acid[86,87]. A stock solution of $Ce(SO_4)_2$ was used as cerium (IV) precursor (Sigma-Aldrich). Cations were co-precipitated in their hydroxide form instantly[85]. Then, the mixture was stirred for 30 minutes. The precipitate was washed by centrifugation, twice with water then once in ethanol before being left to dry in an inert glovebox (Ar) for one week to avoid the oxidation of uranium (IV) into uranyl. Thermal conversion of the powder at 700 °C for 4 hours in a reducing atmosphere (Ar - H_2 4.5%) yielded the final oxide $U_{1-x}Ce_xO_{2\pm\delta}$. The supernatant obtained before the washing steps was analyzed by ICP-AES in order to determine the precipitation yield that was systematically found above 99.9% for all cations.

A heterogeneous material $U_{0.92}Ce_{0.08}O_{2\pm\delta}$ was also prepared according to the industrial MIMAS® process used for MOX fuel[88], but adapted to the scale of laboratory experiments. The protocol is illustrated in Fig. 12. Pure UO_2 (synthesized as stated above) and pure CeO_2 were co-milled in a zirconia ball miller for 30 minutes at 25 Hz to obtain the starting master blend $U_{0.75}Ce_{0.25}O_{2\pm\delta}$. Pure CeO_2 was obtained via oxalic precipitation of cerium (III) precursor ($Ce_2(C_2O_4)_3{\cdot}10H_2O$) followed by a thermal treatment in air at 700 °C in order to oxidize cerium (III) into cerium (IV) and to eliminate any residual carbon caused by the thermal degradation of the oxalate ligand[89]. The master blend was analyzed by XRD and BET, before and after being annealed at 1100 °C for 5 hours under reducing atmosphere to reduce its specific surface area. The master blend was finally diluted with pure UO_2 powder in order to reach the desired composition $U_{0.92}Ce_{0.08}O_{2\pm\ \delta}$.

In order to determine the effective mole fractions of U and Ce in the oxides, a small fraction of each powder (10 mg) was taken out to perform dissolution in 4 mol.L^{-1} HNO_3 at 90 °C for at least 48 hours. In the case of the heterogeneous material, this method

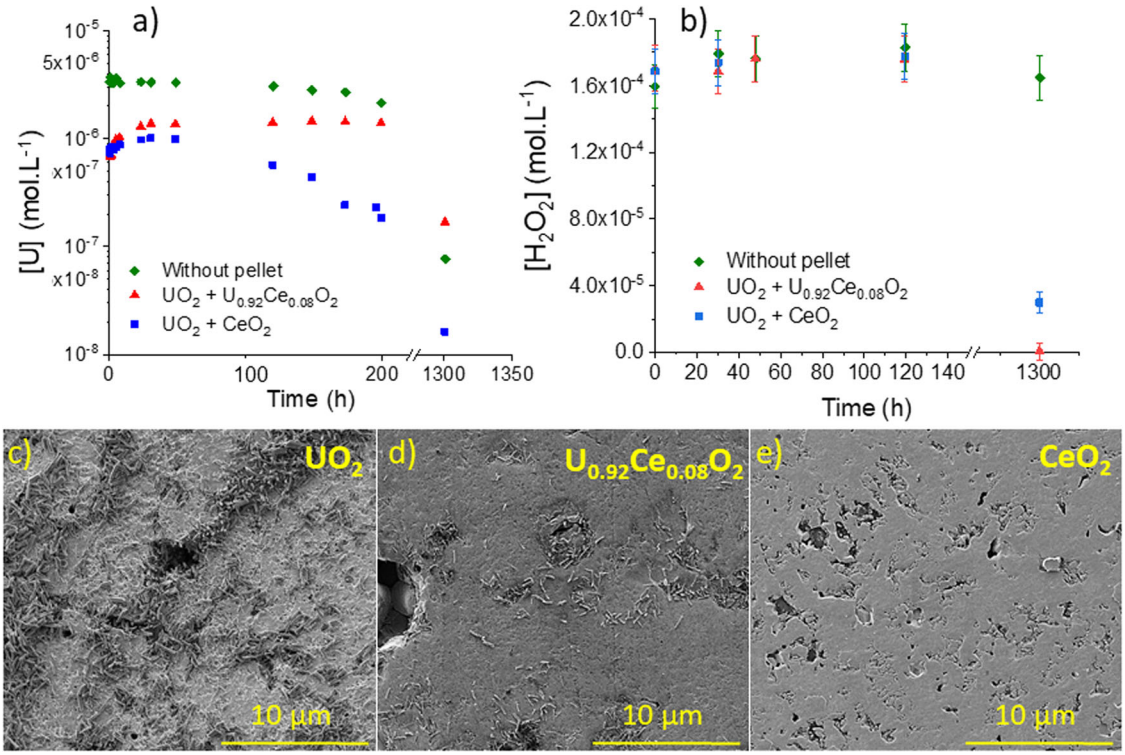

Fig. 11 Evolution of concentrations during static experiments. Evolution of the uranium **a** and $[H_2O_2]$ **b** concentrations during static leaching experiments of $UO_2 + U_{0.92}Ce_{0.08}O_2$ pellets or $UO_2 + CeO_2$ pellets in 0.16 mmol.L^{-1} HCO_3^- solution. SEM micrographs (SE mode) of the surface of the pellets after 1300 h of leaching (**c**, **d**, **e**). Error bars are twice the standard deviation.

did not give reproducible results due to the heterogeneous cationic distribution and to the presence of several phases.

Roughly 180 mg of oxide powder were shaped using a uniaxial pressing for each pellet using a tungsten carbide cylindrical dye. Raw pellets of 5 mm in diameter and densification rate of approximately 50–60% were prepared. Final dense materials were obtained through sintering step at 1600 °C under reducing atmosphere. Dwell time varied between 1 and 5 hours depending on the desired material microstructure and Ce content, in order to obtain a densification rate over 90% and comparable microstructures. Sintered pellets were polished (Buehler Phoenix Beta) on both sides with 10 µm, then 5 µm SiC polishing cloths and finally with a 1 µm diamond paste coating. Polished samples were half cut then annealed at 1000 °C for one hour under reducing atmosphere to remove any oxidized surface layer. Annealed half pellets were stored in an inert glovebox (Ar) until leaching experiments were proceeded.

Characterizations of materials

Raw powders and crushed pellets were analyzed by X-Ray Diffraction (XRD) using a Bruker D8 Advance diffractometer equipped with a Lynx-eye detector and a copper anode X-ray source (Cu $K_{\alpha1,2}$; $\lambda = 1.54184$ Å). XRD patterns were acquired at room temperature within the $5° \leq 2\theta \leq 110°$ angular range and with a step size of 0.02° (corresponding to a total time of roughly 3 hours per sample). To ensure uranium confinement during the analysis, the sample was placed into a hermetically sealed dome-shaped sample holder, with an anti-scattering blade. XRD patterns were refined by the Rietveld method using Cox-Hastings pseudo-Voigt profile function implemented in Fullprof_suite program to determine the cell parameter *a* in the fluorite structure before and after the sintering step. To obtain an acceptable refinement, profile and structures parameters were allowed to vary.

Powder specific surface area were also determined by N_2 adsorption and desorption isotherms at 77 K (BET method) using a Micromeritics ASAP 2020 to compare the relative reactivities of powders toward sintering and to get an average grain size. Prior the analyses, the powdered samples were outgassed at 350 °C during 4 h under vacuum to guarantee that any residual adsorbed water was removed. BET calculation method was applied for P/P_0 where N_2 adsorbed volume was found to be linear.

For each material, a raw pellet was analyzed by dilatometry (Setaram SetSys Evolution) to follow its sintering during the thermal treatment at 1600 °C under reducing atmosphere (Ar – H_2 4.5%). The heating ramp was set to 120 °C.h^{-1} and to 360 °C.h^{-1} for the cooling ramp. The device did not allow maintaining an isotherm plateau at 1600 °C. The results were used to determine the sintering temperature of raw pellets and are shown in Supplementary Fig. 1.

Density of sintered pellets were determined by geometrical measurements associated to helium pycnometry. The geometric measurements were performed using a caliper. 4 measurements of the diameter and of the thickness of the pellet were performed. Assuming a cylindrical geometry, the apparent density of the sample, ρ_{geom} (g.cm^{-3}) was calculated and compared to the theoretical density ρ_{calc} (g.cm^{-3}) of $U_{1-x}Ce_xO_2$ in order to determine the densification rate (expressed in %) and associated total porosity P_{tot} (expressed in %) considering the following equations:

$$\rho_{calc} = \frac{M \times Z}{N_a \times a^3} \quad (4)$$

where M (g.mol^{-1}) is the molar weight of the mixed oxide, Z is the number of formula units per unit cell, N_a is the Avogadro constant and a (cm) is the lattice parameter obtained from crushed sintered pellets XRD patterns refinement.

$$\text{Densification rate} = \frac{\rho_{geom}}{\rho_{calc}} \times 100 = \frac{4m}{\pi\, d^2 h\, \rho_{calc}} \times 100 \quad (5)$$

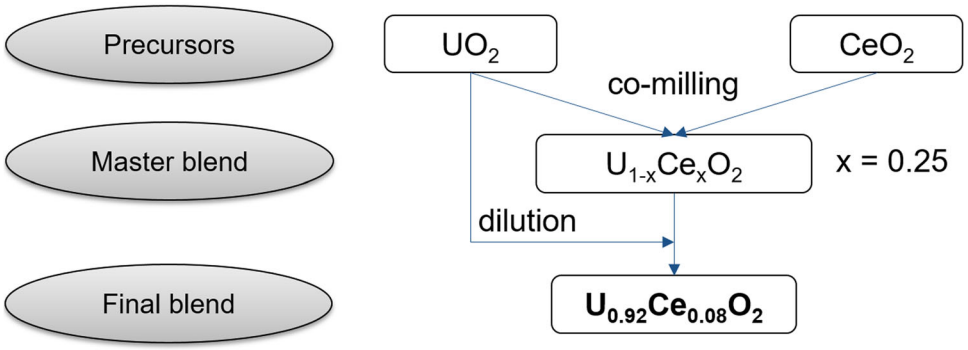

Fig. 12 Preparation of heterogeneous material. Powder metallurgy process used to prepare the heterogeneous $U_{0.92}Ce_{0.08}O_{2\pm\delta}$ material.

where m (g) is the mass, d (cm) is the diameter and h (cm) is the thickness of the pellet.

$$P_{tot} = \left(1 - \frac{\rho_{geom}}{\rho_{calc}}\right) \times 100 \quad (6)$$

Helium pycnometry (Micrometrics, AccuPyc II 1340) was also used to measure the density of the pellets ρ_{pyc} (expressed in g.cm^{-3}) and then to evaluate the closed porosity P_{closed} (expressed in %) as shown in Eq. (7). Ten successive measurements of the pellet volume were achieved. The relative experimental error associated with the density measurements was estimated to 1% and was propagated to determine the relative error on the porosity values.

$$P_{closed} = \left(1 - \frac{\rho_{pyc}}{\rho_{calc}}\right) \times 100 \quad (7)$$

$$P_{open} = \frac{\rho_{pyc} - \rho_{geom}}{\rho_{calc}} \times 100 \quad (8)$$

The microstructural characterization of the pellets was performed by Scanning Electron Microscopy (SEM) using an FEI Quanta 200 apparatus equipped with a backscattered electron detector (BSE) or a secondary electron detector (SE). The samples were observed under vacuum conditions with an acceleration voltage between 5 kV and 25 kV at various magnifications without any metallization step after polishing and annealing. Several images recorded at a magnification of ×5000 were selected at the surface of each sample. The Fiji software was used to bring out the grain boundaries and to binarize the SEM images. Then, with the help of the "analyze particle" plugin, the size distribution of the grains was determined. SEM was also used to characterize the solid/solution interface after the leaching experiment.

Raman spectroscopy analyses were carried out using a LabRam ARAMIS (Horiba Jobin-Yvon) featuring 100x SLMP objective with a numerical aperture of 0.9, yielding a spot size of about 1 µm². The spectrophotometer was furnished with a He-Ne gas 633 nm laser, which was focalized on the sample surface using an Olympus BX 41 microscope. Optical filters were used in order to reduce the power on the sample, thus preventing any sample alteration. In this study, altered samples were cautiously analyzed with an optical filter (D 0.6) with a maximum output power of 1.6 mW while pristine samples were analyzed with a power up to 6 mW. Scattered Raman light emitted by the sample was collected in a 180° backscattering geometry and dispersed by a 1800 grooves.mm^{-1} grating after passing through a 200 µm entrance slit, resulting in a spectral resolution lower than 1 cm^{-1}. For each spectrum, a dwell time of 30–60 s was considered with an average over 3 scans to lower the background. Before analysis, the apparatus was calibrated with a silicon wafer, using the first-order Si line at 520.7 cm^{-1}. 3 to 4 different locations were analysed for each homogeneous sample. For the heterogeneous sample, 4 different locations were analysed for each zone (UO_2 grains and Ce-rich agglomerates, respectively). Once the spectra were acquired, they were processed using PeakFit software. First, a linear baseline correction was used, then the spectra were normalized to the maximum intensity. PeakFit software was then used to fit the bands using Gaussian-Lorentzian functions. The position of the T_{2g} band (between 445 and 465 cm^{-1}) was determined as the centroid of the corresponding peak. Using this method, the standard error (also calculated by PeakFit) associated to the peak position was less than 0.1 cm^{-1}, which was one order of magnitude lower than the spectral resolution. The standard deviation of the T_{2g} positions of spectra recorded at various locations at the sample surface was less than 0.5 cm^{-1}. Thus, an average value for the peak position was calculated and its uncertainty was considered equal to the spectral resolution of the Raman spectrometer, i.e. 1 cm^{-1}.

X-Ray Photoelectron Spectroscopy (XPS) analyses of homogeneous sintered pellets of $U_{1-x}Ce_xO_2$ (with $x = 0$; 0.08; 0.12; 0.25; 1) were carried out with a Thermofisher Escalab 250 XI using a monochromatic Al Kα source ($h\nu$ = 1486.6 eV). Due to charge effects the samples were analyzed using a charge compensation flood gun. The instrument was calibrated to the silver Fermi level (0 eV) and to the $3d_{5/2}$ core level of metallic silver (368.3 eV). The C-1s signal for adventitious carbon was used to correct the charge effect. The C-C/C-H component of C-1s spectra was fixed at 285.0 eV. The spot was 900 µm in diameter. The pass energy for overview and high resolution spectra was 150 eV and 20 eV, respectively. The data processing was performed using the commercial Avantage software. For the fitting procedure, a Shirley background was used.

Leaching experiments

Dynamic leaching experiments were carried out at room temperature over a two-weeks period. The feeding solution flowed through PTFE tubing thanks to a peristaltic pump set to a flow rate of 0.1 mL.min^{-1} into a hermetically closed PTFE reactor containing a half of a pellet and 25 mL of solution. Thus, the residence time of the solution in the reactor was about 4 hours. Downstream from the reactor, a fraction collector sampled automatically and continuously the leachate into 15 mL centrifuge tubes every 100 minutes (10 mL per tube).

Feeding solutions were replaced every 48 h to prevent any advanced H_2O_2 decomposition and thus to maintain a constant concentration during the experiment. To maintain more easily constant conditions during leaching experiments, the carbonate concentration of the feeding solution was the one calculated at equilibrium with air ($pCO_2 = 10^{-3.45}$ atm) at pH 7 and room temperature. Approximately 13 mg of $NaHCO_3$ (Carlo Erba, analytical grade) and 17.2 ± 0.1 µL of H_2O_2 (35 wt.%, Acros Organics, analytical grade, stabilized) were added to 1 L of deionised water. The resulting concentrations of H_2O_2 and

HCO_3^- in the feeding solutions were $(2.0 \pm 0.1) \times 10^{-4}$ mol.L^{-1} and 0.16 mmol.L^{-1}, respectively. The pH of the feeding solution was measured and was systematically found in the range between 6.9 and 7.2.

Selected leachate samples were acidified with 150 µL of HNO_3 15 mol.L^{-1} (69.5%, Sigma-Aldrich, Suprapur®, for trace analysis) in order to get uranium and cerium concentrations. The uranium and cerium elemental concentration was measured using inductively coupled plasma mass spectrometry (ICP-MS, iCAP RQ, Thermo Fisher). The ICP-MS was calibrated for Ce and U elements using several standard solutions prepared by dilution of single element standard solutions at 1000 ppm (PlasmaCAL, SCP Science) in 0.2 mol.L^{-1} HNO_3 solution (Suprapur, for trace analysis Merck). The elemental concentrations of uranium and cerium were calculated as the average of three replicates at each mass (238 and 140). Under these analytical conditions, the detection limit for uranium and cerium reached 1×10^{-10} mol.L^{-1} and 7×10^{-11} mol.L^{-1}, respectively. The relative experimental error was calculated as twice the relative standard deviation of the three replicates and was about 5%.

The leachates were also analyzed in order to determine H_2O_2 concentration using the Ghormley method[90]. Absorbance of the solutions was measured in polypropylene containers at 350 nm using a UV-Vis spectrophotometer (Varian Cary 50 spectrophotometer). The molar extinction coefficient at 350 nm was determined by measuring the absorbance of several standard solutions prepared by dilution of a commercial H_2O_2 solution at 35 wt.% (Sigma-Aldrich, analytical grade, stabilized) in deionized water and was found to be 23600 L.mol^{-1}.cm^{-1}. The detection limit of the analytical procedure was systematically found between 1×10^{-6} -2×10^{-6} mol.L^{-1}. pH, redox potential and dissolved oxygen were also regularly measured in the leachates using InLab® expert Pro pH, InLab® Redox and InLab® Optiox electrodes (Mettler Toledo), respectively. The redox electrode consisted of a Pt electrode combined with an Ag/AgCl reference in 3 mol.L^{-1} KCl electrolyte, a ceramic junction with Ag^+ trap. +207 mV was added to the potential measured with the combined electrode to determine the redox potential, E_h (mV) with respect to the normal hydrogen electrode.

For each experiment, the flow rate and the composition of the leaching solution were kept constant until a steady-state was reached, i.e. until the successive elemental concentrations in the outflow were not significantly different. The normalized alteration rate, expressed in g.m^{-2}.d^{-1}, was then calculated as follows:

$$R_{ss}(i) = \frac{Q}{S \times f_i}(C_i - C_i^{in}) \quad (9)$$

where Q (L.d^{-1}) is the flow rate; C_i^{in} (g.L^{-1}) is the elemental concentration of the element i in the inflow, which equaled zero; S (m^2) is the surface area of the solid in contact with the solution and f_i (g.g^{-1}) is the mass fraction of the element i in the solid. If no secondary phase precipitated during the experiment, this value is equal to the normalized dissolution rate, R_L.

The elemental concentrations at steady state, C_i were determined by averaging the values measured by ICP-MS that were not significantly different considering the experimental error. The expanded uncertainty at 0.95 confidence level on the steady elemental concentration value was estimated as twice the standard deviation of the successive concentration values. The uncertainty on the normalized alteration rate was then estimated by propagating the experimental error on the elemental concentration at steady state.

Moreover, the total alteration thickness $e_i(t)$, expressed in µm, was calculated from $m_i(t)$ (g), the mass of element i released in solution at time t as follows:

$$e_i(t) = \frac{m_i(t)}{f_i \times \rho_{geom} \times S} \quad (10)$$

From the average elemental concentrations and pH values of the leachates, the saturation index of the solution with respect to the studtite was calculated with the geochemical speciation model Phreeqc Interactive (Version 3.3.3)[91]. The solution was considered at equilibrium with air ($pO_2 = 0.2$ atm and $pCO_2 = 10^{-3.5}$ atm). The speciation calculations accounted for the aqueous complexation reactions incorporated in the Thermochimie database[92,93]. The thermodynamic database was completed for the standard solubility product of studtite,$UO_2(O_2) \cdot 4H_2O$(cr) determined by Kutbatko et al.[94] and recommended in the Second Update of Chemical Thermodynamics of Uranium[95], i.e.:

$$UO_2^{2+}(aq) + H_2O_2(aq) + 4H_2O(l) \rightleftarrows UO_2(O_2) \cdot 4H_2O(cr) \quad \log K^\circ = 2.87 \pm 0.02 \quad (11)$$

The activity coefficients were calculated using the Davies equation implemented in the Phreeqc software.

Complementary static leaching experiments were designed to test assumptions. For each experiment, two pellets were placed in the same static leaching reactor (Savillex® type in PFA) with 100 mL of $[H_2O_2]$ solution at $(1.7 \pm 0.1) \times 10^{-4}$ mol.L^{-1} and 0.16 mmol.L^{-1} HCO_3^-. To achieve oversaturated conditions with respect to studtite, uranyl nitrate was added to the reactors to reach a concentration of $[U] = 1.6 \times 10^{-7}$ mol.L^{-1} in the leaching reactors. The pH of the feeding solution was measured and was systematically found in the range between 6.9 and 7.2. The first reactor contained a pellet of UO_2 and a pellet of $U_{0.92}Ce_{0.08}O_2$. The second reactor contained a pellet of UO_2 and a pellet of CeO_2. A blank experiment without pellet was also achieved to follow the evolution of the hydrogen peroxide and uranium concentrations in the absence of pellet. The reactors were continuously stirred during the static leaching experiments. The evolution of the uranium and H_2O_2 concentrations was determined by ICP-AES analyses and UV-vis spectroscopy using the same methods as for the dynamic leaching experiments. After leaching, the pellets were dried in Ar glove box at room temperature and their surface was observed by ESEM.

DATA AVAILABILITY

The datasets generated during and/or analyzed during the current study are available from the corresponding author on reasonable request.

Received: 5 July 2022; Accepted: 31 March 2023;
Published online: 21 April 2023

REFERENCES

1. Ewing, R. C. Long-term storage of spent nuclear fuel. *Nat. Mater.* **14**, 252–257 (2015).
2. Shoesmith, D. W. Fuel corrosion processes under waste disposal conditions. *J. Nucl. Mater.* **282**, 1–31 (2000).
3. Fanghänel, T. et al. Reducing uncertainties affecting the assessment of the long-term corrosion behavior of spent nuclear fuel. *Inorg. Chem.* **52**, 3491–3509 (2013).
4. Sunder, S., Shoesmith, D. W. & Miller, N. H. Prediction of the oxidative dissolution rates of used nuclear fuel in a geological disposal vault due to the alpha radiolysis of water. *MRS Proc.* **353**, 617 (1994).
5. Wu, L., Beauregard, Y., Qin, Z., Rohani, S. & Shoesmith, D. W. A model for the influence of steel corrosion products on nuclear fuel corrosion under permanent disposal conditions. *Corros. Sci.* **61**, 83–91 (2012).
6. Poinssot, C., Ferry, C., Lovera, P., Jegou, C. & Gras, J.-M. Spent fuel radionuclide source term model for assessing spent fuel performance in geological disposal. Part II: matrix alteration model and global performance. *J. Nucl. Mater.* **346**, 66–77 (2005).

7. Eriksen, T. E., Shoesmith, D. W. & Jonsson, M. Radiation induced dissolution of UO_2 based nuclear fuel—a critical review of predictive modelling approaches. *J. Nucl. Mater.* **420**, 409–423 (2012).
8. Clarens, F. et al. The oxidative dissolution of unirradiated UO_2 by hydrogen peroxide as a function of pH. *J. Nucl. Mater.* **345**, 225–231 (2005).
9. Muzeau, B. et al. Radiolytic oxidation of UO_2 Pellets Doped with Alpha-Emitters (238/239Pu). *J. Alloy. Compd.* **467**, 578–589 (2009).
10. Clarens, F. et al. Formation of studtite during the oxidative dissolution of UO_2 by hydrogen peroxide: a SFM study. *Environ. Sci. Technol.* **38**, 6656–6661 (2004).
11. Odorowski, M. et al. Effect of metallic iron on the oxidative dissolution of UO_2 doped with a radioactive alpha emitter in synthetic callovian-oxfordian groundwater. *Geochim. Cosmochim. Acta* **219**, 1–21 (2017).
12. Spahiu, K., Cui, D. & Lundström, M. The fate of radiolytic oxidants during spent fuel leaching in the presence of dissolved near field hydrogen. *Radiochim. Acta* **92**, 625–629 (2004).
13. Cui, D., Low, J. & Spahiu, K. Environmental behaviors of spent nuclear fuel and canister materials. *Energy Environ. Sci.* **4**, 2537 (2011).
14. Cui, D., Low, J., Rondinella, V. V. & Spahiu, K. Hydrogen catalytic effects of nanostructured alloy particles in spent fuel on radionuclide immobilization. *Appl. Catal., B* **94**, 173–178 (2010).
15. Broczkowski, M. E., Noël, J. J. & Shoesmith, D. W. The inhibiting effects of hydrogen on the corrosion of uranium dioxide under nuclear waste disposal conditions. *J. Nucl. Mater.* **346**, 16–23 (2005).
16. Broczkowski, M. E., Zagidulin, D., Shoesmith, D. W. The role of dissolved hydrogen on the corrosion/dissolution of spent nuclear fuel. In *ACS Symposium Series*; (eds. Wai, C. M., Mincher, B. J.) 1046, 349–380 (American Chemical Society, Washington, DC, 2010).
17. Amme, M. et al. Effects of Fe(II) and hydrogen peroxide interaction upon dissolving UO_2 under geologic repository conditions. *Environ. Sci. Technol.* **39**, 221–229 (2005).
18. Fors, P., Carbol, P., Van Winckel, S. & Spahiu, K. Corrosion of high burn-up structured UO_2 fuel in presence of dissolved H_2. *J. Nucl. Mater.* **394**, 1–8 (2009).
19. Ekeroth, E. & Jonsson, M. Oxidation of UO_2 by radiolytic oxidants. *J. Nucl. Mater.* **322**, 242–248 (2003).
20. McNamara, B., Buck, E. & Hanson, B. Observation of studtite and metastudtite on spent fuel. *MRS Proc.* **757**, II9.7 (2002).
21. McNamara, B., Hanson, B. D., Buck, E. C. & Soderquist, C. Corrosion of commercial spent nuclear fuel. 2. radiochemical analyses of metastudtite and leachates. *Radiochim. Acta* **93**, 169–175 (2005).
22. Hanson, B. D. et al. Corrosion of commercial spent nuclear fuel. 1. Formation of studtite and metastudtite. *Radiochim. Acta* **93**, 159–168 (2005).
23. Corbel, C. et al. Increase of the uranium release at an UO_2/H_2O interface under He^{2+} ion beam irradiation. *Nucl. Instrum. Methods Phys. Res., Sect. B* **179**, 225–229 (2001).
24. Corbel, C. et al. Addition versus radiolytic production effects of hydrogen peroxide on aqueous corrosion of UO_2. *J. Nucl. Mater.* **348**, 1–17 (2006).
25. Burns, P. C. & Hughes, K.-A. Studtite, $[(UO_2)(O_2)(H_2O)_2](H_2O)_2$: the first structure of a peroxide mineral. *Am. Mineral.* **88**, 1165–1168 (2003).
26. Burns, P. C. Nanoscale uranium-based cage clusters inspired by uranium mineralogy. *Miner. Mag.* **75**, 1–25 (2011).
27. Oudinet, G. et al. Characterization of plutonium distribution in MIMAS MOX by image analysis. *J. Nucl. Mater.* **375**, 86–94 (2008).
28. Brémier, S., Haas, D., Somers, J. & Walker, C. T. Large area quantitative X-Ray mapping of $(U,Pu)O_2$ nuclear fuel pellets using wavelength dispersive electron probe microanalysis. *Spectrochim. Acta, Part B* **58**, 651–658 (2003).
29. Carbol, P., Fors, P., Van Winckel, S. & Spahiu, K. Corrosion of irradiated MOX fuel in presence of dissolved H_2. *J. Nucl. Mater.* **392**, 45–54 (2009).
30. Odorowski, M. et al. Oxidative dissolution of unirradiated mimas MOX fuel (U/Pu oxides) in carbonated water under oxic and anoxic conditions. *J. Nucl. Mater.* **468**, 17–25 (2016).
31. Kerleguer, V. et al. The mechanisms of alteration of a homogeneous $U_{0.73}Pu_{0.27}O_2$ MOx fuel under alpha radiolysis of water. *J. Nucl. Mater.* **529**, 151920 (2020).
32. Korzhavyi, P. A., Vitos, L., Andersson, D. A. & Johansson, B. Oxidation of plutonium dioxide. *Nat. Mater.* **3**, 225–228 (2004).
33. Markin, T. L. & Street, R. S. The uranium-plutonium-oxygen ternary phase diagram. *J. Inorg. Nucl. Chem.* **29**, 2265–2280 (1967).
34. Markin, T. L., Street, R. S. & Crouch, E. C. The uranium-cerium-oxygen ternary phase diagram. *J. Inorg. Nucl. Chem.* **32**, 59–75 (1970).
35. Nawada, H. P. et al. Oxidation and phase behaviour studies of the U-Ce-0 system. *J. Nucl. Mater.* **139**, 19–26 (1986).
36. Maji, D., Ananthasivan, K., Venkatakrishnan, R., Desigan, N. & Pandey, N. K. Synthesis, characterization and sintering of nanocrystalline $(U_{1-y}Ce_y)O_{2\pm x}$. *J. Nucl. Mater.* **547**, 152824 (2021).
37. Dörr, W., Hellmann, S. & Mages, G. Study of the formation of UO_2-PuO_2 solid solution by means of UO_2-CeO_2 simulate. *J. Nucl. Mater.* **140**, 7–10 (1986).
38. Harrison, R. W. et al. Spark plasma sintering of $(U,Ce)O_2$ as a MOx nuclear fuel surrogate. *J. Nucl. Mater.* **557**, 153302 (2021).
39. Kim, H. S. et al. Applicability of CeO_2 as a surrogate for PuO_2 in a MOX fuel development. *J. Nucl. Mater.* **378**, 98–104 (2008).
40. Desigan, N. et al. Dissolution behaviour of simulated MOX nuclear fuel pellets in nitric acid medium. *Prog. Nucl. Energy* **116**, 1–9 (2019).
41. Desigan, N., Ganesh, S. & Pandey, N. K. Dissolution behavior of fast reactor MOX nuclear fuel pellets in nitric acid medium. *J. Nucl. Mater.* **554**, 153077 (2021).
42. Ziouane, Y., Milhau, T., Maubert, M., Arab-Chapelet, B. & Leturcq, G. Dissolution kinetics of CeO 2 powders with different morphologies and analogy to PuO_2 dissolution. *Hydrometallurgy* **177**, 205–213 (2018).
43. Vanýsek, P., CRC Handbook of Chemistry and Physics. 91st Edition, (ed. W. M. Haynes). (CRC Press, Bocca Raton, FL. 2610, 2010).
44. Shannon, R. D. Revised effective ionic radii and systematic studies of interatomic distances in halides and chalcogenides. *Acta Crystallogr., Sect. A* **32**, 751–767 (1976).
45. Keramidas, V. G. & White, W. B. Raman spectra of oxides with the fluorite structure. *J. Chem. Phys.* **59**, 1561–1562 (1973).
46. Marlow, P. G., Russell, J. P. & Hardy, J. R. Raman scattering in uranium dioxide. *Philos. Mag.* **14**, 409–410 (1966).
47. Livneh, T. & Sterer, E. Effect of pressure on the resonant multiphonon Raman scattering in UO_2. *Phys. Rev. B* **73**, 085118 (2006).
48. Elorrieta, J. M. et al. Laser-induced oxidation of UO $_2$: a Raman study. *J. Raman Spectrosc.* **49**, 878–884 (2018).
49. Chang, I. F. &Mitra, S. S. Application of amodified random-element-isodisplacement model to long-wavelength optic phonons of mixed crystals. *Phys. Rev.* **172**, 924–933 (1968).
50. Peterson, D. L., Petrou, A., Giriat, W., Ramdas, A. K. & Rodriguez, S. Raman scattering from the vibrational modes in $Zn_{1-x}Mn_xTe$. *Phys. Rev. B* **33**, 1160–1165 (1986).
51. Elorrieta, J. M. et al. Pre- and post-oxidation Raman analysis of $(U, Ce)O_2$ oxides. *J. Nucl. Mater.* **508**, 116–122 (2018).
52. Desgranges, L. et al. Miscibility gap in the U–Nd–O phase diagram: a new approach of nuclear oxides in the environment? *Inorg. Chem.* **51**, 9147–9149 (2012).
53. Le Guellec, M. et al. Grain size analysis and characterization by Raman spectroscopy of a homogeneous sintered MOX fuel. *J. Eur. Ceram. Soc.* **42**, 7553–7560 (2022).
54. Medyk, L. et al. Determination of the plutonium content and O/M ratio of (U,Pu) O_{2-x} using Raman spectroscopy. *J. Nucl. Mater.* **541**, 152439 (2020).
55. Bastians, S., Crump, G., Griffith, W. P. & Withnall, R. Raspite and Studtite: Raman Spectra of Two Unique Minerals. *J. Raman Spectrosc.* **35**, 726–731 (2004).
56. Colmenero, F., Bonales, L. J., Cobos, J. & Timón, V. Study of the thermal stability of studtite by in situ Raman spectroscopy and DFT calculations. *Spectrochim. Acta, Part A* **174**, 245–253 (2017).
57. Bartlett, J. R. & Cooney, R. P. On the determination of uranium-oxygen bond lengths in dioxouranium(VI) compounds by Raman spectroscopy. *J. Mol. Struct.* **193**, 295–300 (1989).
58. Thompson, N. B. A. et al. The thermal decomposition of studtite: analysis of the amorphous phase. *J. Radioanal. Nucl. Chem.* **327**, 1335–1347 (2021).
59. Casas, I. et al. Determination of UO_2(s) dissolution rates in a hydrogen peroxide medium as a function of pressure and temperature. *J. Nucl. Mater.* **375**, 151–156 (2008).
60. Pablo, J. D., Casas, I., Clarens, F., Aamrani, F. E. & Rovira, M. The effect of hydrogen peroxide concentration on the oxidative dissolution of unirradiated uranium dioxide. *MRS Proc.* **663**, 409 (2000).
61. Cornelis, G. et al. Solubility and batch retention of CeO_2 nanoparticles in soils. *Environ. Sci. Technol.* **45**, 2777–2782 (2011).
62. Seminko, V. et al. Mechanism and dynamics of fast redox cycling in cerium oxide nanoparticles at high oxidant concentration. *J. Phys. Chem. C.* **125**, 4743–4749 (2021).
63. Yu, P., Hayes, S. A., O'Keefe, T. J., O'Keefe, M. J. & Stoffer, J. O. The phase stability of cerium species in aqueous systems. *J. Electrochem. Soc.* **153**, C74 (2006).
64. Yu, P. & O'Keefe, T. J. The phase stability of cerium species in aqueous systems. *J. Electrochem. Soc.* **153**, C80 (2006).
65. Hayes, S. A., Yu, P., O'Keefe, T. J., O'Keefe, M. J. & Stoffer, J. O. The phase stability of cerium species in aqueous systems. *J. Electrochem. Soc.* **149**, C623 (2002).
66. Johnson, J.; Anderson, F.; Parkhurst, D. L. Database Thermo.Com.V8.R6.230, Rev 1.11. (Lawrence Livermore National Laboratory, California, 2000).
67. Scholes, F. H., Soste, C., Hughes, A. E., Hardin, S. G. & Curtis, P. R. The role of hydrogen peroxide in the deposition of cerium-based conversion coatings. *Appl. Surf. Sci.* **253**, 1770–1780 (2006).
68. Scholes, F. H., Hughes, A. E., Hardin, S. G., Lynch, P. & Miller, P. R. Influence of hydrogen peroxide in the preparation of nanocrystalline ceria. *Chem. Mater.* **19**, 2321–2328 (2007).

69. Campbell, C. T. & Peden, C. H. F. Oxygen vacancies and catalysis on ceria surfaces. *Science* **309**, 713–714 (2005).
70. Pirmohamed, T. et al. Nanoceria exhibit redox state-dependent catalase mimetic activity. *Chem. Commun.* **46**, 2736 (2010).
71. Kim, J.-G., Ha, Y.-K., Park, S.-D., Jee, K.-Y. & Kim, W.-H. Effect of a trivalent dopant, Gd^{3+}, on the oxidation of uranium dioxide. *J. Nucl. Mater.* **297**, 327–331 (2001).
72. Casella, A., Hanson, B. & Miller, W. The effect of fuel chemistry on UO_2 dissolution. *J. Nucl. Mater.* **476**, 45–55 (2016).
73. Park, K. & Olander, D. R. Defect models for the oxygen potentials of gadolinium- and europium-doped urania. *J. Nucl. Mater.* **187**, 89–96 (1992).
74. Grandstaff, D. E. A kinetic study of the dissolution of uraninite. *Econ. Geol.* **71**, 1493–1506 (1976).
75. Demkowicz, P. A. et al. Aqueous dissolution of urania-thoria nuclear fuel. *Nucl. Technol.* **147**, 157–170 (2004).
76. Alliot, C., Grambow, B. & Landesman, C. Leaching behaviour of unirradiated high temperature reactor (HTR) UO_2–ThO_2 mixed oxides fuel particles. *J. Nucl. Mater.* **346**, 32–39 (2005).
77. Heisbourg, G., Hubert, S., Dacheux, N. & Ritt, J. The kinetics of dissolution of $Th_{1-x}U_xO_2$ solid solutions in nitric media. *J. Nucl. Mater.* **321**, 141–151 (2003).
78. Claparede, L. et al. Dissolution of $Th_{1-x}U_xO_2$: effects of chemical composition and microstructure. *J. Nucl. Mater.* **457**, 304–316 (2015).
79. Dalger, T. et al. Kinetics of dissolution of $Th_{0.25}U_{0.75}O_2$ sintered pellets in various acidic conditions. *J. Nucl. Mater.* **510**, 109–122 (2018).
80. Hanken, B. E., Stanek, C. R., Grønbech-Jensen, N. & Asta, M. Computational study of the energetics of charge and cation mixing in $U_{1-x}Ce_xO_2$. *Phys. Rev. B* **84**, 085131 (2011).
81. Bera, S. et al. XPS analysis of $U_xCe_{1-x}O_{2\pm\delta}$ and determination of oxygen to metal ratio. *J. Nucl. Mater.* **393**, 120–125 (2009).
82. Eloirdi, R. et al. X-Ray photoelectron spectroscopy study of the reduction and oxidation of uranium and cerium single oxide compared to (U-Ce) mixed oxide films. *Appl. Surf. Sci.* **457**, 566–571 (2018).
83. Al-Salik, Y., Al-Shankiti, I. & Idriss, H. Core level spectroscopy of oxidized and reduced $Ce_xU_{1-x}O_2$ materials. *J. Electron. Spectrosc. Relat. Phenom.* **194**, 66–73 (2014).
84. Sarrasin, L. et al. Studtite formation assessed by Raman spectroscopy and ^{18}O isotopic labeling during the oxidative dissolution of a MOX fuel. *J. Phys. Chem. C.* **125**, 19209–19218 (2021).
85. Martinez, J. et al. An original precipitation route toward the preparation and the sintering of highly reactive uranium cerium dioxide powders. *J. Nucl. Mater.* **462**, 173–181 (2015).
86. Dacheux, N., Brandel, V. & Genet, M. Synthesis and characterization of mixed valence uranium orthophosphate: $U(UO_2)(PO_4)_2$. *N. J. Chem.* **19**, 15–25 (1995).
87. Dacheux, N., Brandel, V. & Genet, M. Synthesis and properties of uranium chloride phosphate tetrahydrate: $UClPO_4$, $4H_2O$. *N. J. Chem.* **19**, 1029–1036 (1995).
88. Konings, R. J. M.; Stoller, R. *Comprehensive Nuclear Materials* **2**; Elsevier Science, (2020). ISBN: 978-0-08-056033-5.
89. Claparede, L. et al. Multiparametric dissolution of thorium–cerium dioxide solid solutions. *Inorg. Chem.* **50**, 11702–11714 (2011).
90. Charlot, G. Les Méthodes de La Chimie Analytique - Analyse Quantitative Minérale, Edition V.; Masson et Cie Ed., Paris, (1966).
91. Parkhurst, D. L. & Appelo, C. A. J. User's Guide to PHREEQC (Version 2): A Computer Program for Speciation, Batch-Reaction, One-Dimensional Transport and Inverse Geochemical Calculations; U.S.G.S. Water-Resources Investigations Report 99-4259 (1999).
92. Giffaut, E. et al. Andra thermodynamic database for performance assessment: ThermoChimie. *Appl. Geochem.* **49**, 225–236 (2014).
93. Grivé, M., Duro, L., Colàs, E. & Giffaut, E. Thermodynamic data selection applied to radionuclides and chemotoxic elements: an overview of the ThermoChimie-TDB. *Appl. Geochem.* **55**, 85–94 (2015).
94. Kubatko, K.-A. H., Helean, K. B., Navrotsky, A. & Burns, P. C. Stability of peroxide-containing uranyl minerals. *Science* **302**, 1191–1193 (2003).
95. OECD Nuclear Energy Agency. Second Update on the Chemical Thermodynamics of Uranium, Neptunium, Plutonium, Americium and Technetium, *Chemical Thermodynamics*, 14, OECD NEA, ed. (OECD Nuclear Energy Agency, 2021).

ACKNOWLEDGEMENTS

This study was financially supported by a research program funded unitedly by the CEA, EDF and ANDRA. The authors are thankful to the personnel of the ICSM for their technical support, especially R. Podor and J. Lautru for their meticulous work with ESEM and EDS analyses.

AUTHOR CONTRIBUTIONS

T.M.: investigation; data curation; writing—original draft—review and editing. S.S.: conceptualization; methodology; data curation; validation; writing—original draft—review and editing, supervision. V.B.: conceptualization; methodology; validation. P-H.I.: investigation; data curation. S.M.: data curation; validation. F.T.: project administration; funding acquisition, writing—original draft. C.M.: project administration; funding acquisition, writing—original draft. F.M.: investigation; data curation; writing—original draft. C.J.: conceptualization; methodology; data curation; validation; writing—original draft, supervision. N.D.: conceptualization; writing original draft, supervision.

COMPETING INTERESTS

The authors declare no competing interests.

ADDITIONAL INFORMATION

Supplementary information The online version contains supplementary material available at https://doi.org/10.1038/s41529-023-00348-3.

Correspondence and requests for materials should be addressed to Stéphanie Szenknect or Christophe Jégou.

Reprints and permission information is available at http://www.nature.com/reprints

Publisher's note Springer Nature remains neutral with regard to jurisdictional claims in published maps and institutional affiliations.